SAND2018-4540J

NCOMMS-16-19781-T, Nakatsutsumi et al.

Self-generated surface magnetic fields inhibit laser-driven sheath acceleration of high-energy protons

Authors: M. Nakatsutsumi[1,2,4⊥], Y. Sentoku[3,5], A. Korzhimanov[6], S. N. Chen[1,6], S. Buffechoux[1], A. Kon[3,7*], B. Atherton[8], P. Audebert[1], M. Geissel[8], L. Hurd[1†], M. Kimmel[8], P. Rambo[8], M. Schollmeier[8], J. Schwarz[8], M. Starodubtsev[6], L. Gremillet[9], R. Kodama[3,4,7], and J. Fuchs[1,6א]

Affiliations

[1]LULI - CNRS, École Polytechnique, CEA: Université Paris-Saclay; UPMC Univ Paris 06: Sorbonne Universités - F-91128 Palaiseau cedex, France

[2]European XFEL, Holzkoppel 4, 22869 Schenefeld, Germany

[3]Institute of Laser Engineering, Osaka University, Suita, Osaka 565-0871, Japan

[4]Open and Transdisciplinary Research Initiatives, Osaka University, Suita, Osaka 565-0871, Japan

[5]Department of Physics, University of Nevada, Reno, Nevada 89557, USA

[6]Institute of Applied Physics, 46 Ulyanov Street, 603950 Nizhny Novgorod, Russia

[7]Graduate School of Engineering, Osaka University, Suita, Osaka 565-0871, Japan

[8]Sandia National Laboratories, Albuquerque, NM 87123, USA

[9]CEA, DAM, DIF, F-91297 Arpajon, France

⊥,א Correspondence to: Motoaki Nakatsutsumi (motoaki.nakatsutsumi@xfel.eu) and Julien Fuchs (julien.fuchs@polytechnique.fr)

* present address: Japan Synchrotron Radiation Research Institute, Sayo, Hyogo 679-5198, Japan

† present address: Department of Physics and Astronomy, Clemson University, Clemson, South Carolina 29634, USA

Abstract

High-intensity lasers interacting with solid foils produce copious numbers of relativistic electrons, which in turn create strong sheath electric fields around the target. The proton beams accelerated in such fields have remarkable properties, enabling ultrafast radiography of plasma phenomena or isochoric heating of dense materials. In view of longer-term multidisciplinary purposes (*e.g.* spallation neutron sources or cancer therapy), the current challenge is to achieve proton energies well in excess of $100\ \mathrm{MeV}$, which is commonly thought to be possible by raising the on-target laser intensity. Here, we present experimental and numerical results demonstrating that magnetostatic fields self-generated on the target surface may pose a fundamental limit to sheath-driven ion acceleration for high enough laser intensities. Those fields can be strong enough ($\sim 10^5$ T at laser intensities $\sim 10^{21}$ W cm^{-2}) to magnetize the sheath electrons and deflect protons off the accelerating region, hence degrading the maximum energy the latter can acquire.

PACS numbers: 52.38.Ph, 52.38.Kd, 52.65.Rr, 52.38.Dx

Introduction

In the search to increase the energy of proton and ion beams accelerated by intense lasers from solid targets [1], significant work has been devoted to investigating the ion energy scaling with laser [2,3,4,5,6,7,8,9] and target [10,11,12,13,14,15,16,17,18] parameters (see also Supplementary Note 4). In the frame of the most investigated acceleration mechanism, *i.e.* target-normal-sheath-acceleration (TNSA), which is driven by laser-generated electrons, empirical formulas and analytical models [3,4,5,7,19,20,21,22] have been used to obtain the sought-after scaling. These models have been found adequate for $I_{\mathrm{L}}\lambda_{\mathrm{L}}^2 < 10^{20}\,\mathrm{W}\,\mu\mathrm{m}^2\mathrm{cm}^{-2}$ (where I_{L} and λ_{L} are the laser intensity and wavelength, respectively) [2,4,23], but they appear to severely overestimate the measured proton energies at higher intensities [5]. This discrepancy has been attributed to their reduced geometry (usually 1D) or to simplistic assumptions about the plasma dynamics (*e.g.*, isothermal or adiabatic). By contrast, particle-in-cell (PIC) numerical codes provide a first-principles description of the laser-driven ion acceleration process [24,25], yet computational constraints restrict current simulations to rather limited spatio-temporal domains and/or reduced dimensionality. Despite these shortcomings, there has been anticipation of exceeding the 100 MeV energy threshold via TNSA at laser intensities in the $10^{21}\,\mathrm{W}\,\mu\mathrm{m}^2\mathrm{cm}^{-2}$ range.

Most of these studies, however, have overlooked a potentially important factor: the feedback effect on the electrons and accelerating ions of magnetic (B) fields that are self-generated on the target surfaces [25] and can act detrimentally on the particle dynamics for high enough laser intensities. Recently, mounting experimental evidence [26,27,28,29,30] has been obtained showing that tens of MegaGauss (MG) strength B-fields grow in a few 100 fs [28,29] on the target surfaces for $I_{\mathrm{L}}\lambda_{\mathrm{L}}^2 \geq 10^{19}\,\mathrm{W}\,\mu\mathrm{m}^2\mathrm{cm}^{-2}$. Moreover, we have shown that, for laser pulses with a high temporal contrast, a condition that is sought in order to irradiate ultra-thin targets, and hence increase the electron sheath density and the accelerated ion energy [6,9,10,11,15], the surface B-fields are maintained over durations (tens of ps) much longer [29] than the timescale of energy transfer from the electrons to the ions (typically less than 1 ps [4,19]). The potentially detrimental effect of the B-fields on ion acceleration had been evoked in a 3D PIC simulation study [25], but up to now little attention has been paid to it, likely because the MG-strength B-fields observed at present-day laser intensities do not indeed impact ion acceleration.

Here we show that when irradiating targets beyond $10^{20}\,\mathrm{W}\,\mu\mathrm{m}^2\mathrm{cm}^{-2}$ in laser intensity, which is here achieved using a tightly focused laser [31], B-fields of the order of 100 MG (10^4 T) can grow on the target surfaces. Inductive in nature, they arise from the steep transverse gradient of the sheath electric

field accelerating the ions, and hence may continuously affect the cloud of electrons and ions expanding from the target. At even higher laser intensities ($> 10^{21}$ W μm^{2}cm^{-2}), these B-fields can grow to the GigaGauss (GG) level. The electrons subjected to such extreme fields become trapped on the target surface, where they further undergo an $\mathbf{E} \times \mathbf{B}$ drift away from the sheath axis. The resulting inhibition of the electron forward motion is found to hamper the proton acceleration. In addition, part of the protons is significantly deflected outwards, thus degrading the proton beam's exceptional emittance [1]. But we also find that using very short laser pulses (a few tens of fs) might be a way to mitigate the magnetic inhibition effect under consideration since, in such conditions, the protons can be accelerated promptly enough before the electron trajectories are strongly perturbed by the B-fields. The magnetization effect highlighted in our study should be carefully considered when designing ion sources at the upcoming multi-PW laser facilities [32], in particular those with $>$ 100 fs duration [33]. Indeed, extrapolating the existing empirical or theoretical scalings to high-intensity conditions may lead to considerable overestimation of the proton energies, especially for not ultra-short laser pulses.

Results

Magnetic-fields in relativistic laser-solid interaction

Figure 1 shows the spatial distribution of the quasistatic B-fields (B_z) observed in 2D PIC simulations (see Methods) performed at peak laser intensities $I_\mathrm{L}\lambda_\mathrm{L}^2 = 6.5 \times 10^{19}$ W μm^{2}cm^{-2} (Fig. 1a) and 2×10^{21} W μm^{2}cm^{-2} (Fig. 1e). These fields mainly develop on the target surfaces and are polarized normal to the 2D simulation plane. In an actual 3D geometry, as already observed [28,29], they are toroidal and oriented clock-wise around the target normal. Their transverse profile presents a steep increase in strength towards the center, up to the edge of the narrow central region where it abruptly vanishes and changes sign. They are stronger at the rear surface compared to the front, consistently with our previous measurements also performed at high temporal contrast [29], and they reach strengths of about 100 MG and 500 MG, respectively (see also Fig.2a). There, the weak-field region occupies only a small fraction of the ~ 40 μm transverse extent of the electron sheath [34].

These magnetostatic fields are predominantly driven by the currents associated with the laser-driven hot electrons [35,36,37], the same ones responsible for building up the ion accelerating sheath (the protons being preferentially accelerated due to their lowest charge-to-mass ratio). The hot electrons are injected into the target with kinetic energies of several MeV for the laser intensities considered here (see Methods). When exiting the target, a small fraction of them escape into the vacuum [38], but most are

retained by the electrostatic potential barrier, and hence form sheaths on the target surfaces [1]. The inductive generation of the B-field is mainly determined by the spatio-temporal variations of the longitudinal sheath field: $\partial B_z/\partial t \sim \partial E_x/\partial y$ [39] (see Methods). For the sake of simplicity, and consistently with the 2D PIC simulations, this equation is written in 2D geometry. The B-field rapidly grows during the laser irradiation and eventually saturates, an upper limit being reached when the magnetic and electron pressures become comparable: $B_{\max}^2/2\mu_0 \approx n_{\mathrm{h,rear}} k_{\mathrm{B}} T_0$, where T_0, $n_{\mathrm{h,rear}}$ are the hot electrons' initial temperature and density (at the target rear), k_{B} is the Boltzmann constant and μ_0 denotes the vacuum permeability. This should be considered as an upper limit since, as soon as the electrons become magnetized, a further rise in the B-field strength requires a similar rise in $n_{\mathrm{h,rear}}$, which is increasingly difficult to achieve. This scaling predicts that $B_{\max}$ can exceed 0.5 GG at laser intensities $\geq 10^{21}$ W μm^2 cm^{-2}, which is supported by the simulation shown in Fig. 1e (see also Fig. 2a).

Model for plasma expansion and magnetic-field generation

To determine in which measure the B-fields depicted in Fig. 1a,e are detrimental to proton acceleration from the target rear, we resort to a simple 1D analytical model of the temporal evolution of the particles and fields (see Methods). The use of a 1D model is justified provided that the acceleration length of the protons does not exceed the lateral extent of the sheath [23]). The electron temperature, $T_{\mathrm{e}}(t)$, is assumed to evolve as $T_{\mathrm{e}}(t) = T_0$ during $0 \leq t \leq \tau_{\mathrm{L}}$ and $T_{\mathrm{e}}(t) = T_0(\tau_{\mathrm{L}}/t)^2$ for $t > \tau_{\mathrm{L}}$ to mimic adiabatic cooling [20]. The model yields the longitudinal electrostatic field, $E_x(t)$, from which we evaluate the magnetostatic field, $B_z(t)$, as well as the proton front position, $x_{\mathrm{front}}(t)$, and the maximum ion velocity, $v_{\mathrm{p}}(t) = \dot{x}_{\mathrm{front}}(t)$. These quantities are plotted in Fig. 1b,f. The magnetization level can be assessed from comparison of $x_{\mathrm{front}}(t)$ with the typical values of the electron and proton Larmor radii, $R_{\mathrm{L}}^{\mathrm{e,p}}(t)$ (see Methods): the particles can be considered strongly magnetized in the cloud if $R_{\mathrm{L}}^{\mathrm{e,p}}/x_{\mathrm{front}} < 1$. For a laser intensity of 6.5×10^{19} W μm^{2}cm^{-2}, Fig. 1c shows that the electrons become magnetized in ~ 100 fs after the start of the plasma expansion (and during the laser pulse irradiation). When increasing the laser intensity to 2×10^{21} W μm^{2}cm^{-2}, as shown in Fig. 1g, not only do the electrons get strongly magnetized even more quickly, but the protons turn out to be strongly magnetized too during the laser pulse. While this 1D analytical model does not integrate the feedback of the magnetization on the particle cloud expansion and proton acceleration, it clearly indicates that B-fields are likely to impact the electron and proton dynamics at high laser intensity. Complementarily, Fig. 1d,h show the trajectories of sample electrons in the PIC simulation for the two intensities considered (see also Supplementary Note 2,

Supplementary Fig. 2, Supplementary Fig. 3, Supplementary Table 1 and Supplementary Table 2 for modeling of electron trajectories). In agreement with the model predictions, these trajectories show that the electrons are magnetized, drifting away from the center of the sheath, due to the combined actions of the B-field gradient and the $\mathbf{E} \times \mathbf{B}$ drive, the effect being aggravated with the laser intensity.

The main effect of the B-field on the electrons is, by scattering them outward along the target surface, to reduce the longitudinal electron pressure and density (see also Supplementary Note 1 and Supplementary Fig. 1), which shortens the electron sheath and decreases the E-field strength. As for the protons, they tend to be deflected outwards, *i.e.*, towards lower-sheath-field regions, also hampering the energy gain they could expect. Overall, the ion acceleration process is changed from a quasi-1D geometry (neglecting the intrinsic divergence of the hot electrons, which is valid during most of the ion acceleration phase [23]) into a pronounced, less efficient, 3D one. Another expected detrimental effect of the B-field is the inward force exerted by the fluid-like magnetic pressure on the target surface, which tends to counteract the accelerating TNSA field.

Laser intensity dependence of magnetization effects

Figure 2 quantifies the impact of the magnetic field on the particle dynamics as a function of the laser intensity, for fixed values of the laser spot size (1.6 μm), duration (700 fs) and wavelength (1 μm). Figure 2a plots the B-field strength vs. laser intensity as predicted by our 1D model. This theoretical scaling is consistent with the PIC simulation results presented above. Also plotted are experimental data taken from Refs. [27,28,29,30]. Note that these data are not all acquired using the same spot size, but as detailed in Supplementary Note 6 and Supplementary Fig. 7, the dependence of the B-field strength on the laser focal spot at a given intensity is actually rather weak. This is due to the fact that the sheath transverse gradient (responsible for the B-field generation) is dominated by fast recirculation and transverse spread of the hot electrons before the ions have time to move. This holds as long as the laser spot size is smaller than the transverse sheath size (of the order of $40\,\mu$m, see Fig. 1a,e and Supplementary Note 6). Figure 2b plots the particle magnetization parameter at the time of the laser peak, as calculated using the same 1D model as above. This graph demonstrates that the magnetization level increases with the laser intensity. Although electron magnetization starts already for relatively low laser intensities, strong proton magnetization also starts to kick in if one goes to high intensity, *i.e.*, $I_{\mathrm{L}}\lambda_{\mathrm{L}} \sim 10^{21}\,\mathrm{W\,\mu m^2 cm^{-2}}$. As mentioned above, the B-field then deflects protons and damages the beam emittance, one of the outstanding features of TNSA protons [1]. We note that since the highest-energy ions are accelerated on axis where the B-field vanishes, the impact of the B-field upon them is harder to

assess. However, the transverse motion of these on-axis ions is unstable, so that they may be rapidly deflected by the B-field. Finally, note that the electrons will be effectively less magnetized for ultra-short duration lasers (*i.e.,* below 100 fs): this is predominantly due to the short plasma expansion during the laser pulse, so that the electrons experience weaker deflections relative to the sheath extent (Supplementary Note 6,7).

Evidence for magnetization effects at high laser intensity

The above considerations suggest that self-generated B-fields are likely to impact proton acceleration increasingly when raising the laser intensity. To test this, we conducted two experiments (see Methods) geared toward investigating proton acceleration under tight focus conditions in order to maximize the laser intensity, thus falling within the parameter range of Fig. 1 and Fig. 2. This was achieved by means of re-focusing ellipsoidal plasma mirrors (EPM [31,40], see Methods and the setup shown in the inset of Fig. 3).

Figure 3 summarizes the maximum proton energy recorded in these experiments (see open symbols) as a function of the peak laser intensity over three orders of magnitude, up to $1.3 \times 10^{21}\ \mathrm{W}\,\mu\mathrm{m}^2\mathrm{cm}^{-2}$. The experimental data are fairly well reproduced by 2D PIC simulations (see filled symbols) performed in the same conditions. The solid lines plot the results of the 1D plasma expansion model employed in Fig. 1 and Fig. 2, which neglects magnetization effects. These analytical predictions reasonably agree with the experimental measurements, performed at LULI (blue symbols) and SNL (red symbols), at low laser intensities. However, both 2D PIC simulations and experimental results gradually deviate from the model's predictions when the laser intensity exceeds $10^{21}\ \mathrm{W}\,\mu\mathrm{m}^2\mathrm{cm}^{-2}$: compare the 1D model-predicted solid red line vs. the experimental data (red open circles) and simulations (red filled circles) for intensities above $10^{21}\ \mathrm{W}\,\mu\mathrm{m}^2\mathrm{cm}^{-2}$.

For laser intensities below $10^{20}\ \mathrm{W}\,\mu\mathrm{m}^2\mathrm{cm}^{-2}$, the consistency between the 1D analytical model, the 2D simulations and the experimental measurements indicates that the acceleration is quasi-1D, as already demonstrated in a number of studies [4,23,41]. For higher laser intensities, the progressive deviation between the 1D unmagnetized model on the one side, and the data and 2D simulations on the other side points to increasing multi-dimensional effects. This is consistent with the increasing electron and ion deflections (highlighted in Fig. 1 and Fig. 4) induced by B-fields of growing strength, which can be only modelled in a multi-dimensional geometry. Under our long-pulse conditions, we expect that 2D simulations capture the ion acceleration to relatively good accuracy since the protons should reach their saturation energy within the laser pulse, *i.e.,* during the isothermal acceleration stage [19]. Indeed, as was

shown in Refs. [42,43], differences between 2D and 3D simulations mostly arise during the adiabatic acceleration stage (*i.e.,* after the laser irradiation) for protons that have not already reached their final energy in the isothermal stage.

The perturbations caused to the proton angular distribution by the self-generated B-fields at high laser intensities are illustrated in Fig. 4f-h, which display the angular distribution of the proton beam generated at $I_{\mathrm{L}}\lambda_{\mathrm{L}}^2 = 1.3\times10^{21}\ \mathrm{W}\,\mu\mathrm{m}^2\mathrm{cm}^{-2}$ (see also Fig. 4i-k which present azimuthally-averaged angular lineout of the proton dose distributions observed in the films shown in Fig. 4f-h). It is characterized by a hollow ring structure with the proton flux peaking at a finite angle with respect to the target-rear normal. We stress that this ring pattern is observed only for high protons energies (compare Fig. 4f with Fig. 4g-h), and disappears when lowering the laser intensity (Fig. 4c-e), in which case the protons exhibit the standard bell-shaped profiles expected for TNSA [1]. 2D PICLS simulations performed under comparable conditions confirm that for the highest laser intensity, the proton beam is deflected outward and hollowed out (Fig. 4a,b). Moreover, both simulation and measurements show similar variations of the angular peak with the proton energy range (as shown in Supplementary Note 3 and Supplementary Fig. 4) The measured angular peak allows us to infer the average field experienced by protons in a specific energy range. The deflection angle is given by $\theta = e\langle B\rangle l/m_{\mathrm{p}}v_{\parallel}$, where $\langle B\rangle$ is the average B-field strength, l is the longitudinal extent of the magnetized region and $v_{\parallel}$ is the longitudinal proton velocity. Taking $l \sim 5\ \mu\mathrm{m}$ as suggested by the simulation of Fig. 1e and a typical deflection angle of 12° as suggested by Fig. 4g,j, we deduce that protons of energy $E_p = m_{\mathrm{p}}v_{\parallel}^2/2 = 25\ \mathrm{MeV}$ undergo an average field $\langle B\rangle \sim 0.3\ \mathrm{GG}$. This estimate is in reasonable agreement with the results of both the PICLS simulation and the 1D analytical model (see Fig. 2a).

The observed ring pattern could be potentially attributed to a different effect, such as hole boring [44]. Since thin (1.1 μm thick) gold foils were used as targets, light pressure could be strong enough to bore through the entire thickness of the foil, and disrupt the laminar shape of the sheath field (note, however, that this scenario could not explain the observed proton energy dependency of the ring diameter). To evaluate the effectiveness of this effect, we can derive the hole boring velocity from the conservation of momentum and energy fluxes across the irradiated region: $v_{\mathrm{p}}(t) = [(1+R)I_{\mathrm{L}}(t)\cos\alpha/2m_{\mathrm{i}}n_{\mathrm{i}}c]^{1/2}$, where $\alpha = 23^{\circ}$ is the laser incidence angle on target, R is the laser reflectivity, $m_{\mathrm{i}} = 3.3\times10^{-25}$ kg is the ion mass, and $n_{\mathrm{i}} = 5.9\times10^{22}\ \mathrm{cm}^{-3}$ is the ion density in the case of gold. For a Gaussian laser pulse of peak intensity $I_{\mathrm{L}} = 1.3\times10^{21}\ \mathrm{W\,cm}^{-2}$ and assuming $R = 0.5$ [4], the hole-boring depth is estimated to reach 0.8 μm at the peak of the 800 fs duration pulse,

while it takes another 300 fs for the laser beam to break out through the target rear. At that moment, however, according to the PICLS simulation, proton acceleration is already completed and exhibits a clear signature of magnetic deflections in the sheath field. Finally, note that another alternative scenario [45], which would invoke resistive B-fields to account for similar proton ring structures, would need much thicker targets ($> 100\ \mu$m) to be operative.

Discussion

We will now discuss several strategies to limit the magnetization effects on proton acceleration. First, an important factor is the relative timescale of the B-field growth compared to the proton acceleration timescale (which is of the order of the laser pulse duration). Experimentally, at $I_{\mathrm{L}}\lambda_{\mathrm{L}}^2 = 2 \times 10^{19}\ \mathrm{W}\,\mu\mathrm{m}^2\mathrm{cm}^{-2}$, we have measured that the B-fields grow to their maximum strength over > 100 fs (Fig. 6 in Ref. [29]). In the present investigation, the B-fields were hence strongly impacting the electron dynamics since we used relatively long (> 400 fs) laser pulses. Our PIC simulations (Supplementary Fig. 9) and analytical calculations (Supplementary Fig. 8) suggest that when using very short (< 100 fs) laser pulses, the protons are accelerated quickly enough so that the electron Larmor radius is still larger than the longitudinal sheath extent (*i.e.,* the electrons are weakly magnetized). This would be consistent with the fact that, experimentally, proton acceleration with ultra-short laser pulses seems to display a better scaling vs. laser intensity than with longer pulses (Supplementary Fig. 5). To confirm this, precise *in situ* measurements of the B-field temporal dynamics (*e.g.* using a magneto-optical effect in the XUV wavelength range [30]) at high laser intensities and short pulse durations are needed. Nonetheless, we expect that at very high intensities, even for the shortest pulse durations, the magnetic field strength will unavoidably become large enough that the magnetization effect highlighted here will start to be effective, and hence pose a fundamental limit to laser-based ion acceleration.

We tested in the simulations yet another possible strategy for minimizing the B-fields by using small-width targets (so-called reduced mass targets or RMTs), in which the lateral recirculation of electrons homogenizes the sheath and relaxes its transverse gradient of the longitudinal E-field [13]. However, the B-field is also produced by the longitudinal gradient of the transverse field, $\partial E_y/\partial x$, which is enhanced in the case of RMT due to a higher hot-electron density. As a consequence, our simulation shows no noticeable reduction of the magnetic field amplitude with RMT (see Supplementary Note 8 and Supplementary Fig. 10). This agrees with the trend seen in Fig. 3 (red filled squares): the proton energy is only improved by about $30 - 40$ % (mainly as a result of an increased hot electron density and sheath field) when using $20 \times 20\ \mu\mathrm{m}^2$ wide foils instead of $50 \times 50\ \mu\mathrm{m}^2$ wide foils. Note that in particular

circumstances (e.g. when irradiating the tip of an RMT in the presence of a large scale preplasma [46]), self-generated B-fields can be used to compress the sheath and enhance proton acceleration.

The magnetic inhibition effect highlighted in this study will likely impact not only sheath-accelerated ions, but also alternative ion acceleration schemes, such as relativistic transparency [47] and radiation pressure [12,14,48], that are envisioned to be efficient at even higher laser intensities than discussed here. In principle, radiation pressure acceleration does not require, and even desires to minimize, hot electrons which are at the source of the B-fields investigated here; hence it could be seen to be immune to magnetic inhibition, as supported by simulations of thin targets irradiated by high-contrast, ultra-intense laser pulses (Supplementary Fig. 6). However, as recently shown [14], at high laser intensities, tight laser focusing tends anyway to produce hot electrons, which could reintroduce magnetic inhibition of ion acceleration. Undoubtedly, the impact of this previously overlooked process will need to be taken into account when planning for ion acceleration experiments on next-generation ultra-high intensity laser facilities such as APOLLON, ELI or CALA.

METHODS

Experiments

The experiments investigating proton acceleration from solid targets at high laser intensities were performed at the Laboratoire pour l'Utilisation des Lasers Intenses (LULI, France) and Sandia National Laboratory (SNL, NM, USA). Both employed either direct irradiation of the targets positioned at the laser focus, or refocusing of the laser by an ellipsoidal plasma mirror (EPM) [31,40,52]. In the first case, the laser is focused using an $f/2.7$ off-axis-parabolic (OAP) focusing mirror at LULI ($f/4$ at SNL) to a $4.4 \pm 0.5\ \mu$m ($8 \pm 0.5\ \mu$m at SNL) full-width at half-maximum (FWHM) spot. This "direct shot" configuration leads to on-target peak intensities as high as $I_{\mathrm{L}}\lambda_{\mathrm{L}}^2 = 1.3 \times 10^{19}\ \mathrm{W}\,\mu\mathrm{m}^2\mathrm{cm}^{-2}$ at LULI and $6 \times 10^{19}\ \mathrm{W}\,\mu\mathrm{m}^2\mathrm{cm}^{-2}$ at SNL. The peak intensity, I_{L}, used in this paper is evaluated by assuming a Gaussian profile for the beam within the FWHM spot size ϕ_{L}: $I(r,t) = I_{\mathrm{L}} \exp(-4\ln 2\,(r/\phi_{\mathrm{L}})^2 - 4\ln 2\,(t/\tau_{\mathrm{L}})^2)$, where τ_{L} is the FWHM laser duration (400 fs at LULI and 800 fs at SNL). Using as a practical parameter the laser energy contained in the FWHM spot, E_{L}, one obtains $I_{\mathrm{L}} = 16\left(\frac{ln\,2}{\pi}\right)^{3/2}\frac{E_{\mathrm{L}}}{\phi_{\mathrm{L}}^2\tau_{\mathrm{L}}} \approx 1.66\frac{E_{\mathrm{L}}}{\phi_{\mathrm{L}}^2\tau_{\mathrm{L}}}$. Note that, since the laser pulse durations employed here are not extremely short, all of the above intensity calculations do not depend on spatio-temporal couplings within the laser pulse, which can however affect the intensity distribution of broadband, ultrashort laser pulses [49].

To generate higher intensities on target, EPMs were placed behind the focus of the laser produced by the OAP (see the inset of Fig .3 for the setup). The EPM is designed as an ellipsoid of revolution around its major axis (x), $x^2/a^2 + r^2/b^2 = 1$, where $(a,b) = (3.5, 2.012)$ mm at LULI and $(12.25, 7.0)$ mm at SNL, yielding an eccentricity of $\epsilon = 0.818$. The EPM is made of glass treated with an anti-reflection coating at the laser wavelength. It refocuses the laser with a change in the beam numerical aperture. The final FWHM spot size is then reduced to $0.9 \pm 0.1\ \mu$m at LULI and $1.5 \pm 0.2\ \mu$m at SNL (as measured by a CCD coupled with a microscope objective of numerical aperture NA $= 0.6$), yet at the cost of lowering the beam energy. The laser spot at the EPM focus was measured and optimized before each shot. Taking into account the plasma mirror reflectivity and the reduced encircled energy in the focal spot when the plasma mirror is triggered [31], the peak laser intensities are estimated to attain $9 \times 10^{19}\ \mathrm{W}\,\mu\mathrm{m}^2\mathrm{cm}^{-2}$ at LULI and $1.7 \times 10^{21}\ \mathrm{W}\,\mu\mathrm{m}^2\mathrm{cm}^{-2}$ at SNL. The laser intensity on the EPM surface was of $3 - 5 \times 10^{14}\ \mathrm{W\,cm}^{-2}$, similar in both experiments and corresponding to a cumulated fluence on the EPM surface of $130 - 180\ \mathrm{J\,cm}^{-2}$ around the peak of the

pulse, a standard optimal value for plasma mirrors [50,51]. The expansion velocity of the EPM surface at critical density is estimated to be $c_s \approx \sqrt{Z_{\mathrm{eff}} T_e / A m_p}$, with A the atomic mass, m_p the proton mass and an ionization state $Z_{\mathrm{eff}} / Z = 0.7$, assuming all the electrons except the 1s and 2s of Si and O are ionized [50]. The electron temperature $T_e(t)$ depends on the cumulated fluence [50]. The expansion length of the EPM surface is expected to be slightly larger in the SNL experiment due to longer pulse duration: about $0.07\ \mu$m around the temporal peak and $0.19\ \mu$m at the ending foot of the pulse (800 fs after the peak of the pulse). To evaluate the impact of this expansion on the beam focus after the EPM, we performed ray-trace simulations, assuming that the plasma expands normally to the local EPM surface. With a $0.19\ \mu$m expansion of the reflecting surface, the beam size at the EPM focus increased by $0.2\ \mu$m, which is smaller than the diffraction-limited spot size (the spot size vanishes for zero expansion, as diffraction effects are neglected in these ray-trace calculations). More information on the ray-trace calculations is provided in Supplementary Note 9, Supplementary Fig. 11 and Supplementary Fig. 12. Note also that the paraxial approximation starts to fail in the high-NA operating conditions of the EPM. In this case, and for our laser parameters, the peak intensity of the longitudinal laser electric field at the second focus of the ellipsoid reaches $\sim 10\%$ of that of the transverse laser electric field [52].

Similarly to a plasma mirror [50], the EPM also acts as an ultrafast light reflector that is activated only in the rising edge of the laser pulse, hence leading to high-contrast interaction conditions. To obtain similar high-contrast conditions for the direct shots (and thus allow meaningful comparison of their performance), we made use of frequency-doubled pulses at LULI (i.e., operating at a wavelength of $\lambda_L = 0.528\ \mu$m), and of a planar plasma mirror prior to the laser focus at SNL (operating at the fundamental frequency, $\lambda_L = 1.06\ \mu$m). In the latter case, the planar plasma mirror was positioned 20 mm before the OAP focus to be irradiated at the same fluence level as the EPM.

The targets consisted of $0.5 - 2\ \mu$m thick Al and Au foils at LULI and of $1.1\ \mu$m Au foils at SNL. At LULI, the targets were irradiated at normal incidence ($\alpha = 0°$), while oblique incidence ($\alpha = 23°$) and p-polarization were used at SNL. The required target positioning accuracy ($\sim 1 - 2\ \mu$m) at the EPM focus was provided by the NA = 0.6 microscope objective, combined with piezoelectric motors. The accelerated protons were detected using radiochromic films [1,2] and spectrometers positioned $20 - 30$ mm away from the target.

Analytical model

The analytical 1D model used in Figs. 1-3 is based on the theoretical model developed in Ref. [19], which describes the isothermal and collisionless expansion (along the longitudinal x axis in our case, *i.e.* normal to the target surface) of a plasma into the vacuum, as driven by a population of initial hot electrons' temperature (or energy) T_0 and density at the target surface $n_{\mathrm{h,rear}}$. The plasma expands into the vacuum due to electrons pulling out protons through the space-charge electrostatic field. The hot electrons are generated through the $\mathbf{J}\times\mathbf{B}$ [1] and Brunel [53] mechanisms, with kinetic energies of several MeV for the laser intensities considered here [54,55]. In the present paper, the initial hot-electron temperature was estimated as $k_B T_0 = m_e c^2(\gamma_0 - 1)$, where $\gamma_0 = \pi/2\mathrm{K}(-a_0^2)$ is the mean hot-electron relativistic factor, $a_0 = (I_\mathrm{L}\lambda_\mathrm{L}^2 / 1.37\times10^{18}\ \mathrm{W}\,\mu\mathrm{m}^2\mathrm{cm}^{-2})^{1/2}$ is the normalized laser field and K is the elliptical integral of the first kind. This scaling, suggested by Kluge *et al.* [55], is specifically adapted to the interaction of intense lasers with steep-gradient plasmas, *i.e.,* as is achieved under our high-contrast experimental conditions. Furthermore, we found that this scaling gives the closest match to our numerical simulation results. The hot-electron density at the laser-interaction surface is estimated to be $n_\mathrm{h} \approx 0.5\gamma_\mathrm{h} n_\mathrm{c}$ where $n_\mathrm{c} = \varepsilon_0 m_\mathrm{e}\omega_\mathrm{L}^2/e^2$ is the critical density and $\gamma_\mathrm{h} = a_0/\sqrt{2}+1$ is the relativistic factor derived from one-dimensional energy and momentum flux conservation. Here, the factor 0.5 is introduced to take into account the time-averaged value of γ_h. This gives a total absorbed energy into hot electrons of $E_\mathrm{h,tot} = N_\mathrm{h,tot} k_\mathrm{B} T_0$ where $N_\mathrm{h,tot} = \pi n_\mathrm{h}\phi_\mathrm{L}^2\tau_\mathrm{L} v_\mathrm{e}/4$ assuming $v_\mathrm{e}\sim c$. This results in a laser-to-hot-electron coupling efficiency $E_\mathrm{h,tot}/E_\mathrm{L} \sim 25-40\%$ in the intensity range discussed in this paper. The density at the target rear is $n_\mathrm{h,rear} = n_\mathrm{h}(1 + d r_\mathrm{L}^{-1}\tan\theta)^{-2}$where the target thickness is $d = 2\ \mu$m, $r_\mathrm{L} = \phi_\mathrm{L}/2$ is the laser spot radius on target, and the half-angle electron divergence within the target is $\theta \sim 45°$ [4]. In the model, the initial (maximum) electric field in the sheath is given by $E_0 = \sqrt{n_\mathrm{h,rear} k_\mathrm{B} T_0/\varepsilon_0}$. We extracted the proton energy at $t = \tau_\mathrm{L}$. At that moment, according to the PICLS simulation, proton acceleration is already completed for the case of laser pulse durations we explored here.

The azimuthal magnetic field at the target rear is assumed to be generated by the time-dependent Faraday law, $\partial B_z/\partial t = \partial E_x/\partial y - \partial E_y/\partial x \sim \partial E_x/\partial y$, assuming a 2D geometry with $\mathbf{B} = (0, 0, B_\mathrm{z})$. It leads to steady growth of the magnetic field up to the stage when the magnetic pressure becomes comparable with the plasma pressure. We note that other sources (*e.g.* gradients of density and temperature [29]) may induce magnetostatic fields on the target surfaces, yet these processes occur over time-scales longer than the ion acceleration time scales of interest here. In this frame, assuming a Gaussian transverse profile for the longitudinal sheath field, $E_x(y) = E_0 f(t) e^{-(y/r_y)^2}$, we can

approximate its peak transverse gradient as $(\partial E_x/\partial y)_{\max} \sim E_0 f(t)/r_y$. The inductive B-field is then estimated to be $B_z(t) = (E_0/r_y)\int_0^t f(t')dt'$. We consider here the electric field in the plateau region of the sheath where most of the particles are confined. During the isothermal phase ($0 \le t \le \tau_L$), $f(t) = 2/\sqrt{2e_N + \omega_{pi}^2 t^2}$, $\omega_{pi} = \sqrt{n_{h,rear} e^2/m_p \epsilon_0}$ yields $B_z(t) = \left(E_0/r_y \omega_{pi}\right)\ln\left|a + \sqrt{1+a^2}\right|$, where $a = \omega_{pi} t/\sqrt{2e_N}$. The velocity of the accelerating protons increases as $v_p(t) = 2c_{s0}\ln\left|a(t) + \sqrt{1+a(t)^2}\right|$, and the position of the ion front is then given by $x_{front}(t) = \int_0^t v_p(t')dt'$. After the laser pulse, as the electrons progressively give their energy to the ions and cool down in the expansion, T_e decreases with time (see Fig. 1.b). Last, the electron and proton Larmor radii are calculated using $R_L^p(t) = m_p v_p(t)/eB_z(t)$ and $R_L^e(t) = m_e c\sqrt{\gamma(t)^2 - 1}/eB_z(t)$, where $\gamma(t) = 1 + k_B T_e(t)/m_e c^2$.

Numerical simulations

To analyze the plasma dynamics at play during and following the intense laser irradiation, we resort to particle-in-cell (PIC) numerical codes, which provide a first-principles simulation framework more adequate than magneto-hydrodynamics (MHD) codes. Indeed, MHD is based on the assumptions of quasi-neutrality, small particle Larmor radii and thermal particle distributions. While part of these assumptions may locally hold off axis and inside the expanding electron-ion plasma (where quasi-neutrality holds, the B-field is at its strongest, and the electrons may gyrate with radii smaller than the plasma/field scale-lengths), MHD is invalid at the ion front (where the quasi-neutrality assumption breaks down) and/or around the axis (where the B-field weakens and/or changes sign), that is, in the regions where the maximum ion energies are to be found.

The 2D PIC numerical simulations presented in this work are performed using the PICLS, PICADOR and CALDER codes. PICLS features binary collisions among charged particles and dynamic ionization [26]. Absorbing boundary conditions are used for particles in the transverse direction (*i.e.*, no electron reflux is imposed to represent the actual large transverse size of the target). The target consists of a neutral plasma of electrons and Al^{3+} ions. A 20-nm thick layer of protons is added at the target rear surface to mimic the surface contaminants. The resulting two-layer target can lead to modulations in the low-energy side of the proton spectrum [56], especially if the protons in the contaminant layer are depleted [57,58], but this cannot affect the proton maximum energy [56], the observable on which we concentrate here. The ion density is initialized to 5×10^{22} cm^{-3}, while the electron and ion temperatures are both set to zero. The electron density increases dynamically during the laser irradiation via ionization

processes. The spatial (resp. temporal) resolution was 1/50 of the wavelength (resp. laser oscillation period). The laser focal spot and temporal shape obey Gaussian distributions. The collisionless PICADOR code is run on heterogeneous cluster systems including Xeon Phi coprocessors [59]. The PICADOR simulations use exactly the same parameters as the PICLS simulations, except that they neglect the ionization dynamics (i.e., the ion charge state keeps a constant value, $Z = 3$, during the simulations). The CALDER [61] simulations discussed in Supplementary Note 5 consider fully ionized carbon nanometric foils assuming negligible Coulomb collisions.

Code availability

The Matlab code solving the 1D model used in Figs. 1-3 is available from the corresponding authors upon reasonable request.

Data availability

The data that support the findings of this study are available from the corresponding authors upon reasonable request.

Acknowledgements

We acknowledge the expert support of the ELFIE and Sandia 100 TW laser operation crews and engineering teams. We thank Y. Kuramitsu and G. Revet for useful comments and discussions. This work was supported by grant E1127 from Région Ile-de-France, by CREST Japan Science and Technology, and in part by the Ministry of Education and Science of the Russian Federation under Contract No.14.Z50.31.0007. This project has received funding from the European Union's Horizon 2020 research and innovation programme under grant agreement no 654148 Laserlab-Europe, and was partly done within the LABEX Plas@Par project and supported by Grant No. 11-IDEX-0004-02 and ANR-17-CE30-0026 PiNNaCLE grant from Agence Nationale de la Recherche (France).. The simulations were partially performed on resources provided by the Joint Supercomputer Center of the Russian Academy of Sciences. A. Kon acknowledges support from the JSPS Global COE program. M. N. was partially supported by a JSPS Postdoctoral Fellowship for Research Abroad. Y. S. was supported by the JSPS KAKENHI under Grant No. JP15K21767 and the DOE-OFES under Grant No. DE-SC0008827. L. H. acknowledges support by the NASA Earth and Space Science Fellowship Program under grant NNX13AM28H. Sandia National Laboratories is a multi-mission laboratory managed and operated by National Technology and Engineering Solutions of Sandia, LLC., a wholly owned subsidiary of Honeywell International, Inc., for the U.S. Department of Energy's National Nuclear Security Administration under contract DE-NA0003525. Support was also provided by Sandia's Laboratory Directed Research and Development program. The CALDER simulations were performed using HPC resources at TGCC/CCRT (Grant No. 2013-052707).

Author contributions

M.N., R.K and J.F. designed the project, M.N., S.B., A. Kon, M.G., L.H., P.R., M.Sc and J.F. performed the experiment, M.N., J.F., S.B., and A. Kon analyzed the data, Y.S., A.Kor., and L.G. performed the simulations, B.A., P.A. M.K., J.S., M.St., and R.K. supported the students and the project, M.N., Y.S., A.Kor., S.N.C., L.G. and J.F. wrote the paper. All authors discussed the results and reviewed the paper at its various stages.

Competing financial interests

The authors declare that they have no competing interests as defined by Nature Publishing Group, or other interests that might be perceived to influence the results and/or discussion reported in this article.

Figure legends

Figure 1. Laser-driven magnetic-field generation and resulting particle dynamics.
(**a**,**d**,**e**,**h**) 2D particle-in-cell (PIC) simulation results obtained using the (**a**,**e**) PICLS [26] and (**d**,**h**) PICADOR [59] codes (see Methods). The laser pulse impinges from the left onto a 2-μm thick Al foil, coated on its rear side (located at $x = 12\ \mu$m) with a 20-nm thick proton layer. The laser FWHM spot size $\phi_{\rm L}$, duration $\tau_{\rm L}$, wavelength $\lambda_{\rm L}$ and intensity $I_{\rm L}\lambda_{\rm L}^2$ are, respectively, (**a**,**d**) 1 μm, 400 fs, 0.5 μm, 6.5×10^{19} W μm^{2}cm^{-2} and (**e**,**h**) 1.6 μm, 700 fs, 1 μm and 2×10^{21} W μm^{2}cm^{-2}. (**a**,**e**) Magnetostatic field B_z (in MG units) developing inside and outside the target at 100 fs after the laser peak. (**d**,**h**) Sample electron trajectories from the PIC simulations, exiting the target at the laser peak. In **d**, the electron energies lie in the same range: 13.8 MeV (green), 14.3 MeV (red), 12.3 MeV (blue) and 18.7 MeV (cyan), yet the green electron proves more strongly magnetized because it is ejected into the vacuum about 50 fs later, and thus experiences a higher B-field. In **h**, the electron energies are 25.2 MeV (blue), 27.7 MeV (green), 90.9 MeV (red) and 162.7 MeV (cyan). (**b**,**c**,**f**,**g**) Results from the 1D expansion model (see Methods) at a laser intensity of (**b**,**c**) $I_{\rm L}\lambda_{\rm L}^2 = 6.5\times10^{19}$ W μm^{2}cm^{-2} and (**f**,**g**) $I_{\rm L}\lambda_{\rm L}^2 = 2\times10^{21}$ W μm^{2}cm^{-2} using the corresponding PIC simulation parameters. (**b**,**f**) Time evolutions of the proton velocity, $v_{\rm p}(t)$, normalized to its final value (dashed green line), of the electron temperature, $T_{\rm e}(t)$, normalized to its initial value ($T_0 = 1.1$ MeV in **b** and $T_0 = 5.6$ MeV in **f**, see Methods) (dashed-dotted red line), and of the inductive B-field, normalized to its predicted saturation value $B_{\rm max} \equiv \left(2\mu_0 n_{\rm h,rear} k_{\rm B} T_0\right)^{1/2}$ ($B_{\rm max} = 144$ MG in **b** and $B_{\rm max} = 537$ MG in **f**) (solid blue line). (**c**,**g**) Time evolutions of the electron ($R_{\rm L}^{\rm e}$, blue) and proton ($R_{\rm L}^{\rm p}$, red) radii, normalized to the instantaneous longitudinal extent of the proton plasma, $x_{\rm front}(t)$. The horizontal dashed black line delimitates the boundary between the regimes of strong ($R_{\rm L}^{\rm e,p}/x_{\rm front} < 1$) and weak ($R_{\rm L}^{\rm e,p}/x_{\rm front} > 1$) magnetization. The vertical dashed-dotted line indicates the time when the ion front has moved a distance larger than the local Debye length.

Figure 2: Magnetic field strength and particle magnetization vs. laser intensity.
(**a**) Blue solid curve: magnetic field strength (in MG units) as a function of laser intensity ($I_{\rm L}\lambda_{\rm L}^2$) from the 1D model (see text for details on the parameters) taken at 350 fs after the plasma expansion starts (*i.e.*, corresponding to the temporal peak for the 700 fs pulse). Experimental data are shown as red points ([A] correspond to Ref. [27], [B] to Ref. [29], [C] to Ref. [28], and [D] to Ref. [30]), while PIC simulation

results are shown as blue boxes (see Fig. 1). (**b**) Normalized Larmor radii of electrons ($R_{\mathrm{L}}^{\mathrm{e}}/x_{\mathrm{front}}$, red) and protons ($R_{\mathrm{L}}^{\mathrm{p}}/x_{\mathrm{front}}$, dashed blue), at the laser intensity peak, as predicted by the 1D model. The laser parameters are those of Fig. 1e-h: $\phi_{\mathrm{L}} = 1.6\ \mu\mathrm{m}$, $\tau_{\mathrm{L}} = 700$ fs and $\lambda_{\mathrm{L}} = 1\ \mu\mathrm{m}$.

Figure 3: Experimental maximum proton energy vs. on-target peak intensity ($I_{\mathrm{L}}\lambda_{\mathrm{L}}^2$).

For the LULI experiments (black or blue open symbols), the targets were Al and Au foils of thickness between 0.5 μm and 2 μm and of transverse dimensions $> 1 \times 1\ \mathrm{mm}^2$. For the SNL experiment (red open symbols), the targets were 1.1 μm thick Au foils with transverse dimensions between $50 \times 50\ \mu\mathrm{m}^2$ and $300 \times 300\ \mu\mathrm{m}^2$ (note that no trend on the size was observed). Each point corresponds to a single laser shot. Lines plot predictions of the 1D plasma expansion model considered in Fig. 1 and Fig. 2, and which neglects magnetic field effect (see Methods). Filled symbols represent 2D PICLS simulation results with 2 μm-thick Al targets: filled circles and triangles are for $50 \times 50\ \mu\mathrm{m}^2$ wide targets and filled red squares for $20 \times 20\ \mu\mathrm{m}^2$ wide targets. The error bars on the proton energy quantify the energy range of the radiochromic films used to diagnose the TNSA protons. The error bars in the laser intensity arise from the uncertainty in estimating the encircled laser energy within the FWHM spot. (inset) Experimental setup employing a refocusing ellipsoidal plasma mirror (EPM) to reduce the laser focal spot and increase the laser intensity [31].

Figure 4: Magnetic deflections of protons at high laser intensity.

(**a**,**b**) Maps of the proton energy density (in units of $100\ n_{\mathrm{c}}$ keV, where $n_{\mathrm{c}} = 1.1 \times 10^{21}\mathrm{cm}^{-3}$ is the critical density at 1 μm wavelength) as recorded, at the time of the laser peak, from the 2D PICLS simulations illustrated in Fig. 1a and Fig. 1e, respectively. Panel **b** clearly reveals that at high laser intensity, the protons at the acceleration front are deflected by the magnetic field, forming a ring-like pattern. (**c**-**h**) Experimental 2D proton dose distributions (in Gy units) measured using stacks of calibrated radiochromic films. In **c**-**e,** the laser parameters are $I_{\mathrm{L}}\lambda_{\mathrm{L}}^2 = 9 \times 10^{19}\ \mathrm{W}\,\mu\mathrm{m}^2\mathrm{cm}^{-2}$, $\lambda_{\mathrm{L}} = 0.5\ \mu\mathrm{m}$, $\phi_{\mathrm{L}} = 0.9\ \mu\mathrm{m}$, $\tau_L = 400$ fs, and the target consists of a 0.5 μm thick Al foil. In **f**-**h**, the laser parameters are $I_{\mathrm{L}}\lambda_{\mathrm{L}}^2 = 1.3 \times 10^{21}\ \mathrm{W}\,\mu\mathrm{m}^2\mathrm{cm}^{-2}$, $\lambda_{\mathrm{L}} = 1\ \mu\mathrm{m}$, $\phi_{\mathrm{L}} = 1.5\ \mu\mathrm{m}$, $\tau_L = 800$ fs, and the target is a 1.1 μm thick Au foil, yielding a ring-like pattern on the proton dose distribution, consistent with the simulation shown in **b**. For the > 28 MeV protons, this ring pattern encircles what looks like a central jet, which may result from some high-energy protons emitted on axis and having experienced relatively weak deflections. The white bars in **c**-**h** indicate an angular spread of 20°. (**i**-**k**) Proton dose vs. angle

with respect to the target-rear normal, as extracted from the proton distribution displayed in **f**-**h**, respectively. Arrows indicate the angular peaks.

503 # REFERENCES

1 Macchi, A., Borghesi, M., and Passoni, M. Ion acceleration by superintense laser-plasma interaction. *Reviews of Modern Physics* **85**, 751-793 (2013).

2 Snavely, R. A. *et al*. Intense High-Energy Proton Beams from Petawatt-Laser Irradiation of Solids. *Phys*. *Rev*. *Lett*. **85**, 2945-2948 (2000).

3 Schreiber, J., *et al*. Analytical Model for Ion Acceleration by High-Intensity Laser Pulses. *Phys*. *Rev*. *Lett*. **97**, 045005 (2006).

4 Fuchs, J. *et al*. Laser-driven proton scaling laws and new paths towards energy increase. *Nature Phys*. **2**, 48-54 (2006).

5 Robson, L. *et al*. Scaling of proton acceleration driven by petawatt-laser–plasma interactions. *Nature Phys*. **3,** 58-62 (2006).

6 Ceccotti, *et al*. Proton Acceleration with High-Intensity Ultrahigh-Contrast Laser Pulses. *Phys*. *Rev*. *Lett*. **99**, 185002 (2007).

7 Passoni, M., Bertagna, L. and Zani, A. Energetic ions from next generation ultraintense ultrashort lasers: Scaling laws for Target Normal Sheath Acceleration. *Nucl*. *Inst*. *Methods Phys*. *Res*. *A* **620,** 46 (2010).

8 Green, J. *et al*. Enhanced proton flux in the MeV range by defocused laser irradiation. *New J*. *Phys*. **12**, 085012 (2010).

9 Wagner, F. *et al*. Maximum Proton Energy above 85 MeV from the Relativistic Interaction of Laser Pulses with Micrometer Thick CH2 Targets. *Phys*. *Rev*. *Lett*. **116**, 205002 (2016).

10 Kaluza, M., *et al*. Influence of the Laser Prepulse on Proton Acceleration in Thin-Foil Experiments. *Phys*. *Rev*. *Lett*. **93,** 045003 (2004).

11 Antici, P., *et al*. Energetic protons generated by ultrahigh contrast laser pulses interacting with ultrathin targets. *Phys Plasmas* **14,** 030701 (2007).

12 Henig, A., *et al*. Enhanced Laser-Driven Ion Acceleration in the Relativistic Transparency Regime. *Phys*. *Rev*. *Lett*. **103**, 045002 (2009).

13 Buffechoux, S., *et al*. Hot Electrons Transverse Refluxing in Ultraintense Laser-Solid Interactions. *Phys*. *Rev*. *Lett*. **105,** 015005 (2010).

14 Dollar, F., *et al*. Finite Spot Effects on Radiation Pressure Acceleration from Intense High-Contrast Laser Interactions with Thin Targets. *Phys*. *Rev*. *Lett*. **108**, 175005 (2012)

15 Kim, I. Jong, *et al*. Transition of Proton Energy Scaling Using an Ultrathin Target Irradiated by Linearly Polarized Femtosecond Laser Pulses. *Phys*. *Rev*. *Lett*. **111**, 165003 (2013).

16 Zigler, A., *et al*. Enhanced proton acceleration by an ultrashort laser interaction with structured dynamic plasma targets. *Phys*. *Rev*. *Lett*. **110**, 215004 (2013).

17 Green, J. S., *et al*. High efficiency proton beam generation through target thickness control in femtosecond laser-plasma interactions. *Appl*. *Phys*. *Lett*. **104**, 214101 (2014).

18 Bin, J. H., *et al*. Ion Acceleration Using Relativistic Pulse Shaping in Near-Critical-Density Plasmas. *Phys*. *Rev*. *Lett*. **115**, 064801 (2015).

19 Mora, P. Plasma expansion into a vacuum, *Phys*. *Rev*. *Lett*. **90**, 185002 (2003).

20 Mora, P. Thin-foil expansion into vacuum. *Phys*. *Rev*. *E* **72**, 056401 (2005).

21 Murakami, M., and Basko, M. M. Self-similar expansion of finite-size non-quasi-neutral plasmas into vacuum: Relation to the problem of ion acceleration. *Phys*. *Plasmas* **13**, 012105 (2006).

22 Andreev, A., *et al*. Fast-Ion Energy-Flux Enhancement from Ultrathin Foils Irradiated by Intense and High-Contrast Short Laser Pulses. *Phys*. *Rev*. *Lett*. **101**, 155002 (2008).

23 Chen, S. N., *et al*. Passive tailoring of laser-accelerated ion beam cut-off energy by using double foil assembly. *Phys*. *Plasmas* **21**, 023119 (2014).

24 Esirkepov, T., Yamagiwa, M., and Tajima, T. Laser Ion-Acceleration Scaling Laws Seen in Multiparametric Particle-in-Cell Simulations. *Phys*. *Rev*. *Lett*. **96,** 105001 (2006).

25 Pukhov, A. Three-Dimensional Simulations of Ion Acceleration from a Foil Irradiated by a Short-Pulse Laser. *Phys*. *Rev*. *Lett*. **86**, 3562-3565 (2001).

26 Sentoku, Y., d'Humières, E., Romagnani, L., Audebert, P., and Fuchs, J. Dynamic Control over Mega-Ampere Electron Currents in Metals Using Ionization-Driven Resistive Magnetic Fields. *Phys*. *Rev*. *Lett*. **107**, 135005 (2011).

27 Sarri, G., *et al*. Dynamics of Self-Generated, Large Amplitude Magnetic Fields Following High-Intensity Laser Matter Interaction. *Phys*. *Rev*. *Lett*. **109**, 205002 (2012).

28 Schumaker, W., *et al*. Ultrafast Electron Radiography of Magnetic Fields in High-Intensity Laser-Solid Interactions. *Phys*. *Rev*. *Lett*. **110**, 015003 (2013).

29 Albertazzi, B., *et al*. Dynamics and Structure of Self-generated Magnetics Fields on solids following high contrast, high intensity laser irradiation. *Phys*. *Plasmas* **22**, 123108 (2015).

30 Tatarakis, M., *et al*. Laser technology: Measuring huge magnetic fields. *Nature* **415**, 280 (2002).

31 Nakatsutsumi, M., *et al*. Fast focusing of short-pulse lasers by innovative plasma optics toward extreme intensity. *Opt*. *Lett*. **35**, 2314-2316 (2010).

32 Danson, C., Hillier, D., Hopps, N., and Neely, D. Petawatt class lasers worldwide. *High Power Laser Science and Engineering* **3**, e3 (2015).

33 Weber, S. *et al*. P3: An installation for high-energy density plasma physics and ultra-high intensity laser matter interaction at ELI-Beamlines. *Matter and Radiation at Extremes* **2**, 149-176 (2017).

34 Antici, P., *et al*. Modeling target bulk heating resulting from ultra-intense short pulse laser irradiation of solid density targets. *Phys*. *Plasmas* **20**, 123116 (2013).

35 Bell, A. R., *et al*. Observation of plasma confinement in picosecond laser-plasma interactions. *Phys*. *Rev*. *E* **48**, 2087-2093 (1993).

36 Mason, M. J., and Tabak, M. Magnetic Field Generation in High-Intensity-Laser–Matter Interactions. *Phys*. *Rev*. *Lett*. **80**, 524-527 (1998).

37 Sherlock, M. Generalized Ohm's law for a background plasma in the presence of relativistic charged particles *Phys*. *Rev*. *Lett*. **104,** 205004 (2010).

38 Link, A., Freeman, R. R., Schumacher, D. W., and Van Woerkom, L. D. Effects of target charging and ion emission on the energy spectrum of emitted electrons. *Phys*. *Plasmas* **18**, 053107 (2011).

39 Sentoku, Y. *et al*., Isochoric heating in heterogeneous solid targets with ultrashort laser pulses. *Phys*. *Plasmas* **14**, 122701 (2007).

40 Wilson, R., *et al*. Ellipsoidal plasma mirror focusing of high power laser pulses to ultra-high intensities. *Phys*. *Plasmas* **23**, 033106 (2016).

41 Romagnani, L., et al., Dynamics of electric fields driving laser acceleration of multi–MeV protons. *Phys*. *Rev*. *Lett*. **95**, 195001 (2005).

42 Sgattoni, A., et al., Laser ion acceleration using a solid target coupled with a low-density layer. *Phys*. *Rev*. *E* **85**, 036405 (2012).

43 d'Humières, E. et al., Optimization of laser-target interaction for proton acceleration. *Phys*. *Plasmas* **20**, 023103 (2013).

44 Wilks, S. C., Kruer, W. L., Tabak, M., and Langdon, A. B. Absorption of ultra-intense laser pulses. *Phys*. *Rev*. *Lett*. **69**, 1383-1386 (1992).

45 Clark, E. L., *et al*. Measurements of Energetic Proton Transport through Magnetized Plasma from Intense Laser Interactions with Solids. *Phys*. *Rev*. *Lett*. **84**, 670-673 (2000).

46 Lezhnin, K. V., *et al*. Laser Ion Acceleration from Mass-Limited Targets with Preplasma. *Phys. Plasmas* **23**, 053114 (2016).

47 Lin, L., *et al*. Monoenergetic and GeV ion acceleration from the laser breakout afterburner using ultrathin targets. *Phys. Plasmas* **14**, 056706 (2007).

48 Kar, S., *et al*. Ion Acceleration in Multispecies Targets Driven by Intense Laser Radiation Pressure. *Phys. Rev. Lett.* **109**, 185006 (2012).

49 Pariente, G., et al. Space–time characterization of ultra-intense femtosecond laser beams. *Nature Photonics* **10**, 547–553 (2016).

50 Doumy, G. *et al*. Complete characterization of a plasma mirror for the production of high-contrast ultraintense laser pulses. *Phys. Rev. E* **69**, 026402 (2004).

51 Dromey, B., *et al*. High harmonic generation in the relativistic limit. *Nature Phys*. **2**, 456 (2006).

52 Jeong, T. E., *et al*. Spatio-temporal modification of femtosecond focal spot under tight focusing condition, *Opt. Exp*. **23**, 11641-11656 (2015)

53 Brunel, F. Not-so-resonant, resonant absorption. *Phys. Rev. Lett*. **59**, 52-55 (1987).

54 Haines, M. G., Wei, M. S., Beg, F. N., and Stephens, R. B. Hot-Electron Temperature and Laser-Light Absorption in Fast Ignition. *Phys. Rev. Lett*. **102**, 045008 (2009).

55 Kluge, T., Cowan, T., Debus, A., Schramm, U., Zeil, K., and Bussmann, M. Electron Temperature Scaling in Laser Interaction with Solids. *Phys. Rev. Lett*. **107**, 205003 (2011).

56 Allen, M., *et al.,* Proton spectra from ultraintense laser–plasma interaction with thin foils: Experiments, theory, and simulation. *Phys. Plasmas* **10**, 3283-3289 (2003).

57 Esirkepov, T.Z., *et al.,* Proposed Double-Layer Target for the Generation of High-Quality Laser-Accelerated Ion Beams. *Phys. Rev. Lett*. **89**, 175003 (2002)

58 Hegelich, B., *et al.,* Laser acceleration of quasi-monoenergetic MeV ion beams. *Nature* **439**, 441-444 (2006).

59 Surmin, I. A., *et al*. Particle-in-Cell laser-plasma simulation on Xeon Phi coprocessors. *Comput. Phys. Commun*. **202**, 204-210 (2016)

61 Lefebvre E., *et al*. Electron and photon production from relativistic laser–plasma interactions. Nucl. Fusion **43**, 629-633 (2017)

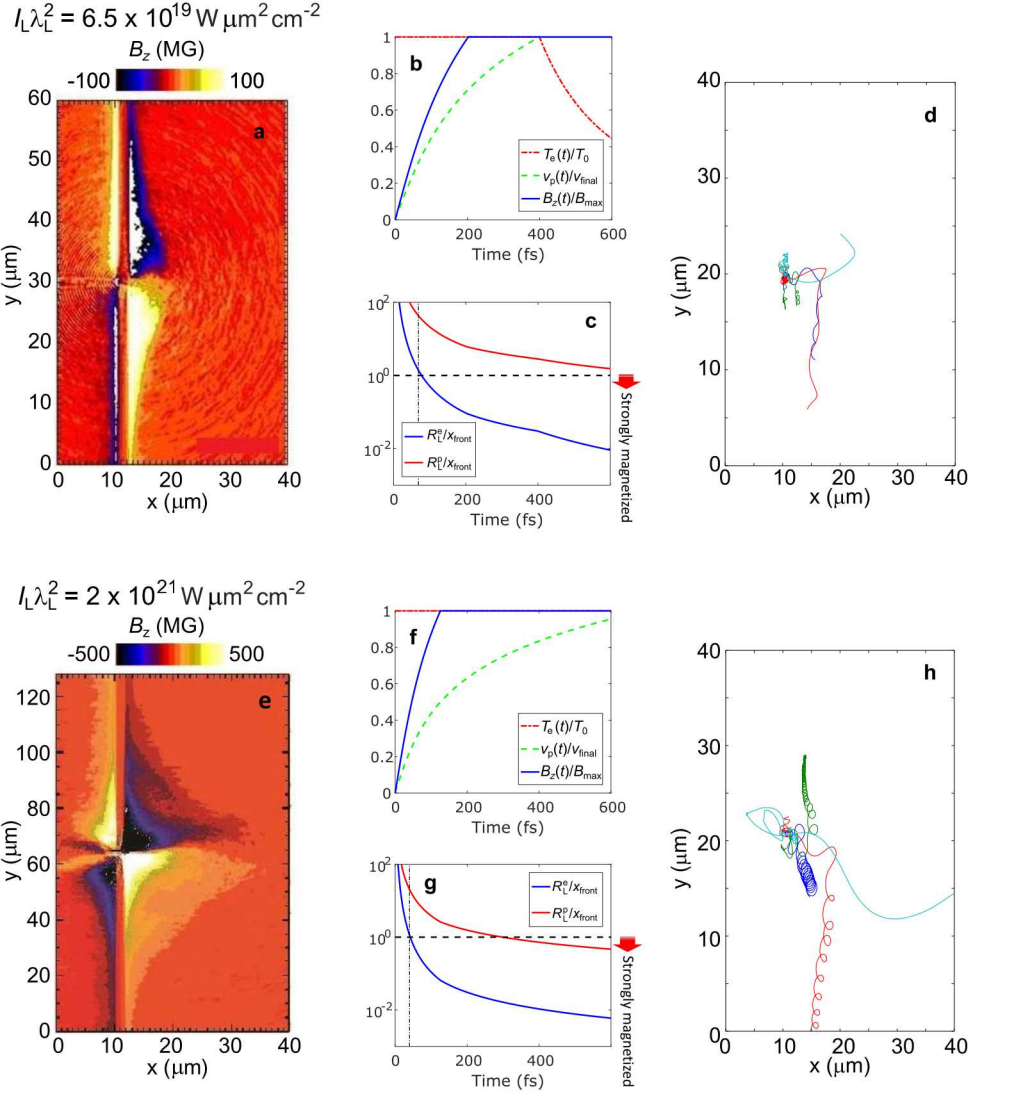
$I_L\lambda_L^2 = 6.5 \times 10^{19}\,W\,\mu m^2\,cm^{-2}$
B_z (MG)
-100
100
a
y (μm)
x (μm)
b
$T_e(t)/T_0$
$v_p(t)/v_{final}$
$B_z(t)/B_{max}$
Time (fs)
c
R_L^e/x_{front}
R_L^p/x_{front}
Strongly magnetized
Time (fs)
d
y (μm)
x (μm)
$I_L\lambda_L^2 = 2 \times 10^{21}\,W\,\mu m^2\,cm^{-2}$
B_z (MG)
-500
500
e
y (μm)
x (μm)
f
$T_e(t)/T_0$
$v_p(t)/v_{final}$
$B_z(t)/B_{max}$
Time (fs)
g
R_L^e/x_{front}
R_L^p/x_{front}
Strongly magnetized
Time (fs)
h
y (μm)
x (μm)

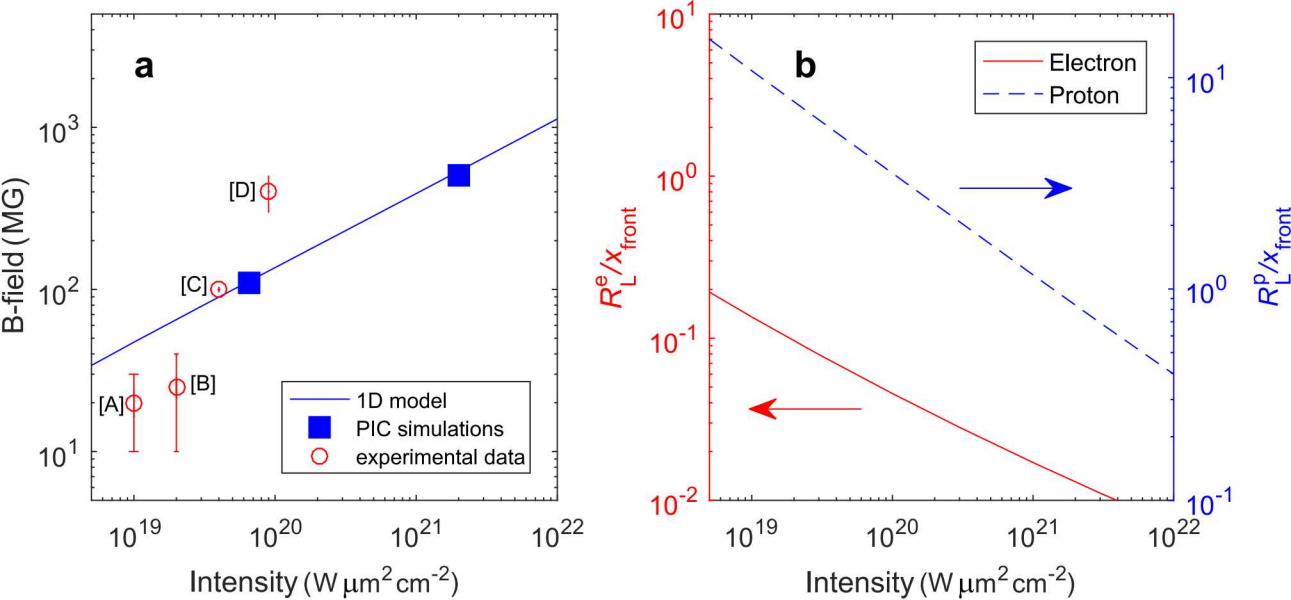
a
B-field (MG)
10^3
10^2
10^1
[A]
[B]
[C]
[D]
1D model
PIC simulations
experimental data
10^{19}
10^{20}
10^{21}
10^{22}
Intensity (W μm² cm⁻²)
b
Electron
Proton
R_L^e/x_{front}
R_L^p/x_{front}
10^1
10^0
10^{-1}
10^{-2}
10^{19}
10^{20}
10^{21}
10^{22}
Intensity (W μm² cm⁻²)

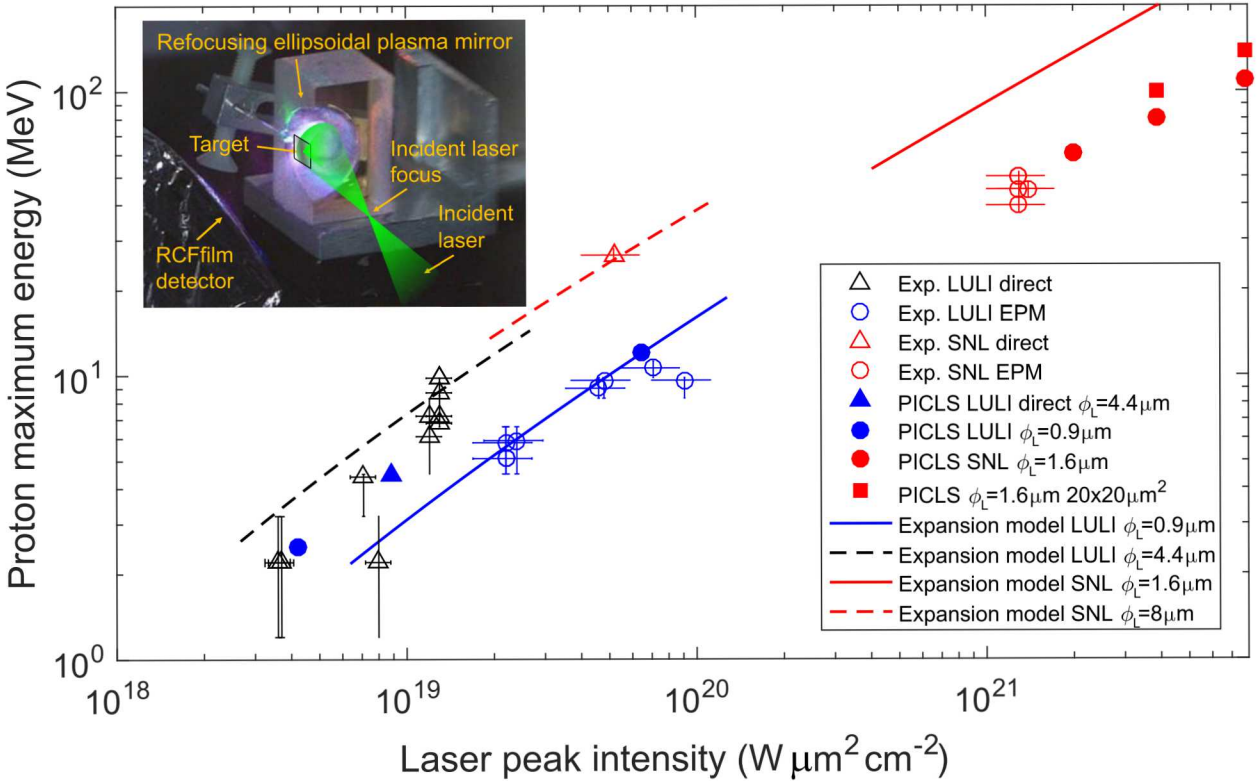
Refocusing ellipsoidal plasma mirror
Target
Incident laser focus
Incident laser
RCFfilm detector
Proton maximum energy (MeV)
Laser peak intensity (W μm² cm⁻²)
Exp. LULI direct
Exp. LULI EPM
Exp. SNL direct
Exp. SNL EPM
PICLS LULI direct φL=4.4μm
PICLS LULI φL=0.9μm
PICLS SNL φL=1.6μm
PICLS φL=1.6μm 20x20μm²
Expansion model LULI φL=0.9μm
Expansion model LULI φL=4.4μm
Expansion model SNL φL=1.6μm
Expansion model SNL φL=8μm

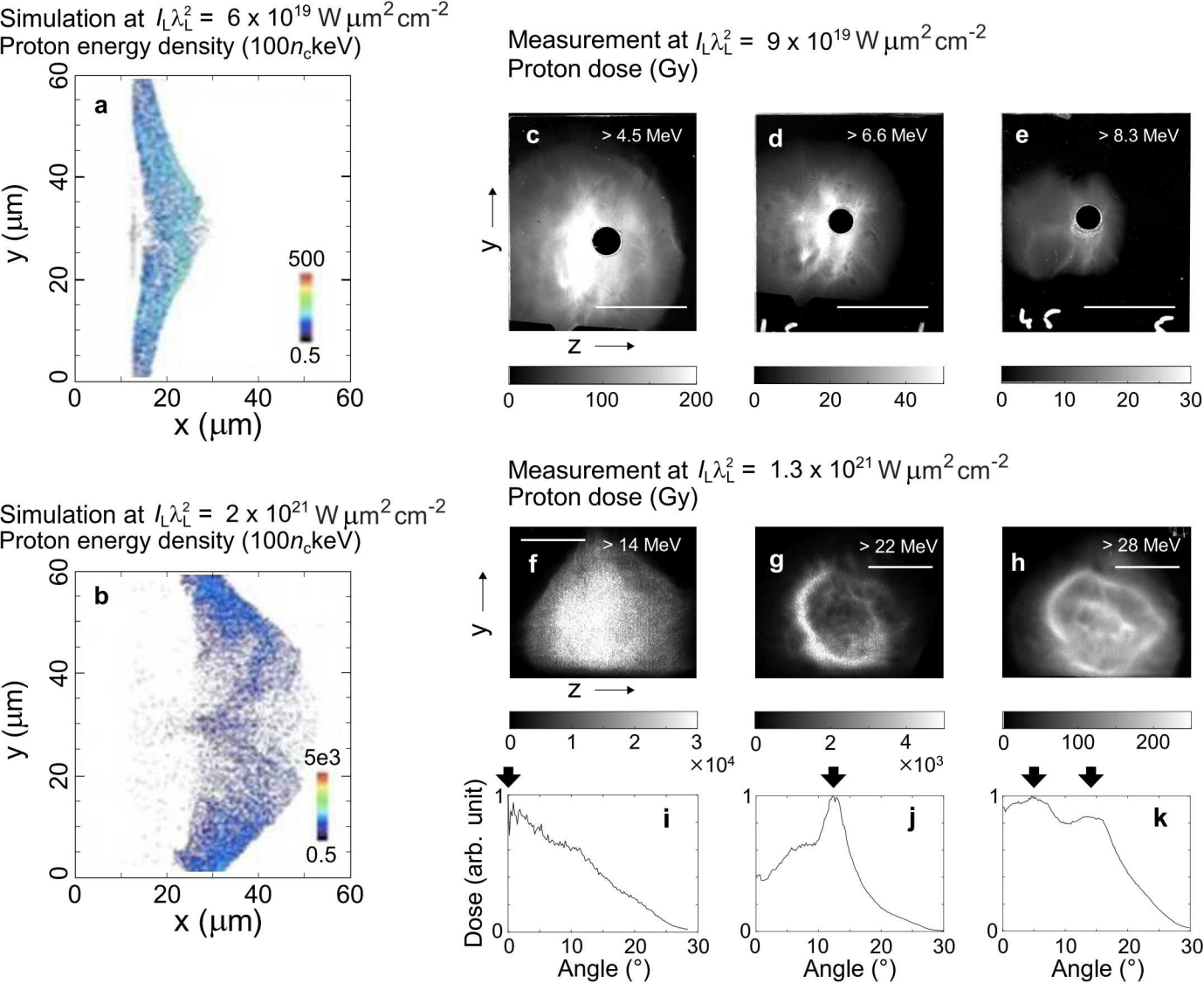
Simulation at $I_L\lambda_L^2$ = 6 x 10^{19} W μm^2 cm^{-2}
Proton energy density (100$n_c$keV)
a
500
0.5
y (μm)
x (μm)
Measurement at $I_L\lambda_L^2$ = 9 x 10^{19} W μm^2 cm^{-2}
Proton dose (Gy)
c > 4.5 MeV
d > 6.6 MeV
e > 8.3 MeV
y
z
Simulation at $I_L\lambda_L^2$ = 2 x 10^{21} W μm^2 cm^{-2}
Proton energy density (100$n_c$keV)
b
5e3
0.5
Measurement at $I_L\lambda_L^2$ = 1.3 x 10^{21} W μm^2 cm^{-2}
Proton dose (Gy)
f > 14 MeV
g > 22 MeV
h > 28 MeV
×10^4
×10^3
Dose (arb. unit)
i
j
k
Angle (°)

Supplementary Note 1: Correlation between regions of strong magnetic fields, electron depletion and proton deflection

Supplementary Figure **1** shows various field and particle distributions from a 2D particle-in-cell (PIC) simulation performed with the PICLS code for a laser intensity $I_{\mathrm{L}} = 6.6 \times 10^{20}\ \mathrm{W\,cm^{-2}}$, a pulse duration of 400 fs, and a wavelength $\lambda_{\mathrm{L}} = 0.5\ \mu\mathrm{m}$ (corresponding to a dimensionless field strength $a_0 = 11$). From the electron energy density (Supplementary Fig. 1c), we observe that, in the population of electrons that are detached from the target (and which were accelerated early on in the laser pulse, before the B-field would reach its maximum strength), there is a strong depletion in the strong-B-field regions [Supplementary Fig. 1b]. We also observe that those electrons crossing the target rear in the late part of the laser pulse are trapped by the magnetic field along the target surface (see the detailed electron trajectories in Fig. 1 of the main text) and are prevented to move forward in the sheath. This disrupts the continuous supply of hot electrons which is crucial for TNSA acceleration to be efficient; by limiting the number of hot electrons within the expanding sheath, the magnetization quenches the ion accelerating electrostatic field earlier than would have taken place otherwise. Note that this is true for such relatively long laser pulses – Supplementary Notes 7 and 8 discuss the benefit brought in this respect by using shorter laser pulses.

The proton energy density displayed in Supplementary Fig. 1d further reveals that the protons at the acceleration front are transversely (and hence angularly as well, see Supplementary Notes 2 and 3 for more details) modulated due to the magnetic field; being deflected outwards, they also move away from the high-sheath-field region, which reduces further the acceleration efficiency. This impresses on them a ring-like pattern that is well consistent with the experimental observations made at high intensity (see Fig. 4 of the main text).

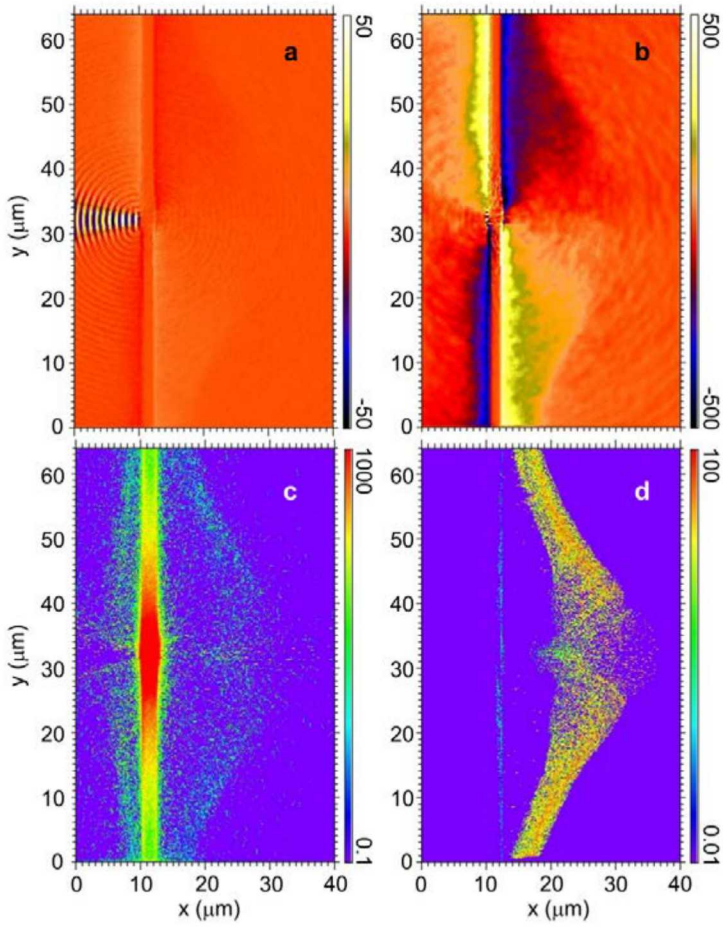

Supplementary Figure 1: Interaction of a tightly focused intense laser with a thin Al foil. 2D PICLS simulation of a laser pulse of 6.6×10^{20} W cm^{-2} intensity, 400 fs FWHM duration, 0.5 μm wavelength and 1.6 μm FWHM spot size interacting with a 2 μm thick Al target. (**a**) Laser electric field (in units of 6.4×10^{12} V m^{-1}) (**b**) Quasistatic magnetic field (in units of 10^6 G). (**c**) Electron energy density (in units of $100n_c$ keV, where $n_c = 1.1 \times 10^{21}$ cm^{-3} is the critical density at 1 μm wavelength. (**d**) Proton energy density (in units of $100n_c$ keV). All snapshots are taken 100 fs after the peak of the laser pulse.

Supplementary Note 2: Modeling particle trajectories inside expanding plasma fields

In complement to Fig. 1 of the main text, it is of interest to analyze the trajectories of electrons and protons inside the strong DC fields generated at the target surfaces. For this purpose, we consider a 2D xy domain, where the x-axis is taken to be parallel to the target rear normal (consistently with the simulations presented in the main text). The electromagnetic field is considered steady, with $\mathbf{E} = (E_x, 0, 0)$ and $\mathbf{B} = (0, 0, B_z)$. A relativistic treatment is considered for the particles, which do not interact between themselves.

The trajectory of a particle of charge q, mass m, position $\mathbf{x}$, velocity $\mathbf{v}$, momentum $\mathbf{p}$ and Lorentz factor γ is defined by the following equations of motion,

$$\frac{dp_x}{dt} = q\left(E_x + v_y B_z\right), \tag{1}$$

$$\frac{dp_y}{dt} = -q v_x B_z, \tag{2}$$

$$v_x = \dot{x} = \frac{p_x}{m\gamma}, \tag{3}$$

$$v_y = \dot{y} = \frac{p_y}{m\gamma}. \tag{4}$$

A particle trajectory starting at $t = t_0$ has as input parameters:

$$\mathbf{p}(t_0) = m_e c\sqrt{\gamma^2(t_0) - 1},$$
$$p_x(t_0) = p(t_0)\cos\theta(t_0),$$
$$p_y(t_0) = p(t_0)\sin\theta(t_0),$$

where we have introduced the initial Lorentz factors, $\gamma_e(t_0) = 1 + \epsilon_{\mathrm{e}}(t_0)[\mathrm{MeV}]/0.511$ for the electrons, and $\gamma_p = 1 + \epsilon_{\mathrm{p}}[\mathrm{GeV}]/0.94$ for the protons, where $\epsilon_{\mathrm{e,p}}$ denotes the kinetic energies. The initial angle with respect to the x axis is taken to be $\theta(t_0) = 0$. The initial velocities, $v_x(t_0)$ and $v_y(t_0)$, are used in Supplementary Eqs. (1) and (2) to yield $\boldsymbol{p}(t_1)$, $\theta(t_1)$ and $\gamma(t_1)$. Then, the particle position is advanced through $\boldsymbol{p}(t_1 - \Delta t)\Delta t/m\gamma(t_1)$. The time step Δt is chosen to be 0.02 fs for electrons and 0.1 fs for protons.

The B-field map shown in Fig. 1a,e of the main text is approximated in the form

$$B_z = -B_0(x)\sin\left(\frac{\pi}{2}\frac{y-y_0}{\Delta y_\mathrm{B}}\right)$$

for $|y-y_0| \le \Delta y_\mathrm{B}$, and in the form

$$B_z = -\mathrm{sgn}(y-y_0)B_0(x)\exp\left(-\frac{|y-y_0|-\Delta y_\mathrm{B}}{L_{y\mathrm{B}}}\right),$$

for $|y-y_0| > \Delta y_\mathrm{B}$. The longitudinal profile is assumed to be

$$B_0(x) = B_\mathrm{max}\exp[-(x-x_0)/L_{x\mathrm{B}}],$$

for $x \ge x_0$ and $B_0(x) = 0$ otherwise. To reproduce the PIC-simulated B-field distributions shown in Fig. 1a,e we set $x_0 = 10\ \mu m$ and $y_0 = 30\ \mu m$, and use the best-fitting values detailed in Supplementary Table 1.

Supplementary Table 1: Best-fitting parameters for the PIC-simulated B-field distributions

	Fig. 1a $I_\mathrm{L}\lambda_\mathrm{L}^2 = 6.5\times10^{19}$ W μm^{2}cm^{-2} $\phi_\mathrm{L} = 1\ \mu$m	Fig. 1e $I_\mathrm{L}\lambda_\mathrm{L}^2 = 2\times10^{21}$ W μm^{2}cm^{-2} $\phi_\mathrm{L} = 1.6\ \mu$m
B_max	100 MG	500 MG
Δy_B	5 μm	6 μm
$L_{x\mathrm{B}}$	4 μm	5 μm
$L_{y\mathrm{B}}$	20 μm	20 μm

Supplementary Table 2: Best-fitting parameters for the PIC-simulated E-field distributions

	Fig. 1.a1 $I_\mathrm{L}\lambda_\mathrm{L}^2 = 6.5\times10^{19}$ W cm$^{-2}\mu$m^2 $\phi_\mathrm{L} = 1\ \mu$m	Fig. 1.b1 $I_\mathrm{L}\lambda_\mathrm{L}^2 = 2\times10^{21}$ W cm$^{-2}\mu$m^2 $\phi_\mathrm{î} = 1.6\ \mu$m
E_max	1 TV m^{-1}	3 TV m^{-1}
Δx_E	0.5 μm	0.5 μm
Δy_E	2 μm	2 μm
L_{xE}	4 μm	5 μm
L_{yE}	20 μm	20 μm

As for the E-field, it is taken in the form

$$E_x(x,y) = E_0(x)$$

for $|y-y_0| \le \Delta y_\mathrm{E}$, and in the form

$$E_x(x,y) = E_0(x)\exp\left(-\frac{|y-y_0| - \Delta y_\mathrm{E}}{L_{y\mathrm{E}}}\right)$$

for $|y-y_0| > \Delta y_\mathrm{E}$. The longitudinal profile is assumed to be

$$E_0(x) = E_\mathrm{max}$$

for $x \le x_0 + \Delta x_\mathrm{E}$, and

$$E_0(x) = E_\mathrm{max}\exp[-(x-x_0-\Delta x_\mathrm{E})/L_{x\mathrm{E}}]$$

otherwise. Moreover, $E_0(x) = 0$ is assumed inside the target ($x < x_0$). The parameters best fitting the simulated E-field results are given in Supplementary Table 2.

Typical particle trajectories are shown in Supplementary Figure **2** ($I_\mathrm{L}\lambda_\mathrm{L}^2 = 6.5 \times 10^{19}\ \mathrm{W}\,\mu\mathrm{m}^2\mathrm{cm}^{-2}$, $\phi_\mathrm{L} = 1\ \mu\mathrm{m}$, $B_\mathrm{max} = 100$ MG) and Supplementary Figure **3** ($I_\mathrm{L}\lambda_\mathrm{L}^2 = 2 \times 10^{21}\ \mathrm{W}\,\mu\mathrm{m}^2\mathrm{cm}^{-2}$, $\phi_\mathrm{L} = 1.6\ \mu\mathrm{m}$, $B_\mathrm{max} = 500$ MG), which correspond to Fig. 1a and Fig. 1e of the main text, respectively. For $B_\mathrm{max} = 100$ MG (Supplementary Figure **2**), electrons of energies in the 10 MeV range suffer strong magnetic deflections, yet still move in the forward direction ($x > 0$). By contrast, protons of a few MeV energies are weakly influenced by the magnetic field. For $B_\mathrm{max} = 500$ MG (Supplementary Figure **3**), the proton trajectories are strongly deflected so that a hollow pattern forms in their spatial distribution. As a result, one of the outstanding features of TNSA protons, namely their high laminarity, is ruined. As for the electrons, their forward motion is severely hampered, most of them being trapped at the target rear surface (consistently with the PIC simulations shown in Supplementary Figure **1**).

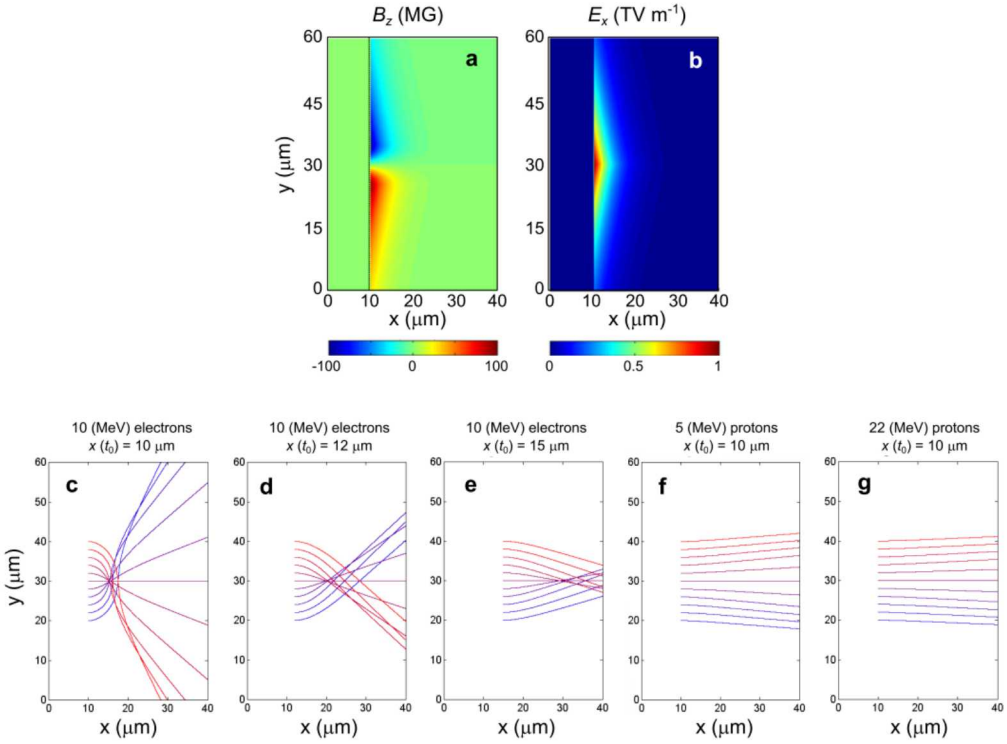

Supplementary Figure 2: Model-predicted fields and particle trajectories at a 6.5×10^{19} W μm^{2}cm^{-2} intensity. (**a**) B_z (in MG units) and (**b**) E_x (in TV m^{-1} units) field maps reproducing the PIC simulation results at an intensity of 6.5×10^{19} W cm^{-2}μm^2 (see Fig. 1a of the main text). The parameters are $B_{\max} = 100$ MG and $E_{\max} = 1$ TV m^{-1}. (**c**-**e**) Trajectories of 10 electrons starting from different initial transverse positions $[y(t_0) - y_0 = -10, -8, -6, \ldots + 10\ \mu m]$ around the symmetry axis $y = y_0$. The initial kinetic energy of the electrons is 10 MeV and they are injected along $x > 0$ at various locations: (**c**) $x(t_0) = x_0$, (**d**) $x(t_0) = x_0 + 2$ μm and (**e**) $x(t_0) = x_0 + 5$ μm. (**f**-**g**) Trajectories of 10 protons starting from $x = x_0$ and different initial y positions $(y(t_0) - y_0 = -10, -8, -6, \ldots + 10\ \mu m)$. The initial kinetic energies of protons are (**f**) 5 MeV and (**g**) 22 MeV, and they are injected along $x > 0$. The symmetry axis is positioned at $y_0 = 30\ \mu$m and $x_0 = 10\ \mu$m is the location of the target rear surface.

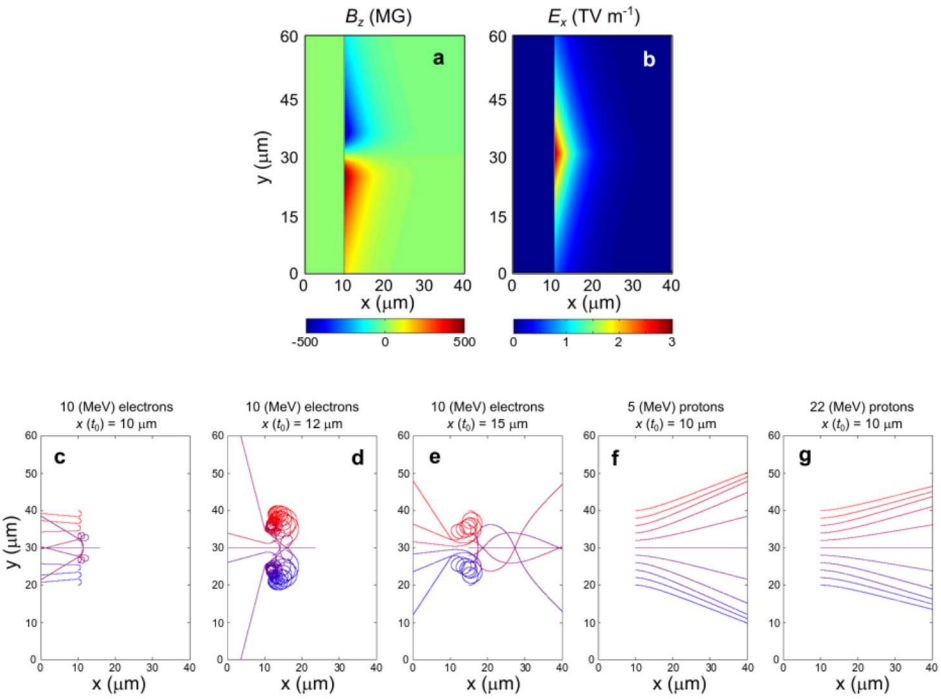

Supplementary Figure 3: Model-predicted fields and particle trajectories at a 2×10^{21} W μm^{2}cm^{-2} intensity. (**a**) B_z (in MG units) and (**b**) E_x (in TV m^{-1} units) maps reproducing the PIC simulation results at an intensity of 2×10^{21} W cm$^{-2}\mu$m^2 (see Fig. 1e of the main text). The parameters are and $B_{\max} = 500$ MG and $E_{\max} = 3$ TV m^{-1}(**c**-**e**) Trajectories of 10 electrons starting from different initial transverse positions $[y(t_0) - y_0 = -10, -8, -6, \ldots + 10\ \mu\text{m}]$ around the symmetry axis $y = y_0$. The initial kinetic energy of the electrons is 10 MeV and they are injected along $x > 0$ at various locations: (**c**) $x(t_0) = x_0$, (**d**) $x(t_0) = x_0 + 2\ \mu$m and (**e**) $x(t_0) = x_0 + 5\ \mu$m. (**f**-**g**) Trajectories of 10 protons starting from $x = x_0$ and different initial y positions ($y(t_0) - y_0 = -10, -8, -6, \ldots + 10\ \mu\text{m}$). The initial kinetic energies of protons are (**f**) 5 MeV and (**g**) 22 MeV, and they are injected along $x > 0$. The symmetry axis is positioned at $y_0 = 30\ \mu$m and $x_0 = 10\ \mu$m is the location of the target rear surface.

Supplementary Note 3: Angle-energy proton distributions

The peaks of the angular distributions measured by the RCF at a laser intensity of $I_{\mathrm{L}}\lambda_{\mathrm{L}}^2 = 1.3 \times 10^{21}$ W μm^2 cm^{-2} and a spot size of $\phi_{\mathrm{L}} = 1.6$ μm (Figs. 4f-h of the main text) exhibit strong dependency on the proton energy. This is summarized in Supplementary Figure 4a, on which is overlaid the angle-energy distribution extracted from the 2D PICLS simulation (red dots). Both experimental and simulated distributions show two distinct proton groups, indicated by lines 1 and lines 2. Line 1 (resp. 2) corresponds to a population of protons with deflection angle increasing (resp. decreasing) with energy. Moreover, the average magnetic field, $\langle B_z \rangle$, seen by protons of a given energy ϵ_{p} as inferred from their measured deflection angle via the relation $\theta = e\langle B_z \rangle l/m_{\mathrm{p}}v_{\parallel}$, is plotted in Supplementary Figure 4 with open blue squares. We have defined $v_{\parallel} = \sqrt{2\epsilon_{\mathrm{p}}/m_{\mathrm{p}}}$ as the longitudinal proton velocity, and l is the longitudinal extent of the magnetized region. We take $l \sim 5$ μm as suggested by the simulated B-field map displayed in Fig. 1e in the main text.

The PIC-simulated angular distributions of the protons are further detailed in Supplementary Figure 4b,c for low- and medium-energy protons. These angular distributions are observed to be quite consistent with the experimental data shown respectively in Fig. 4.g,j and Fig. 4.h,k of the main text.

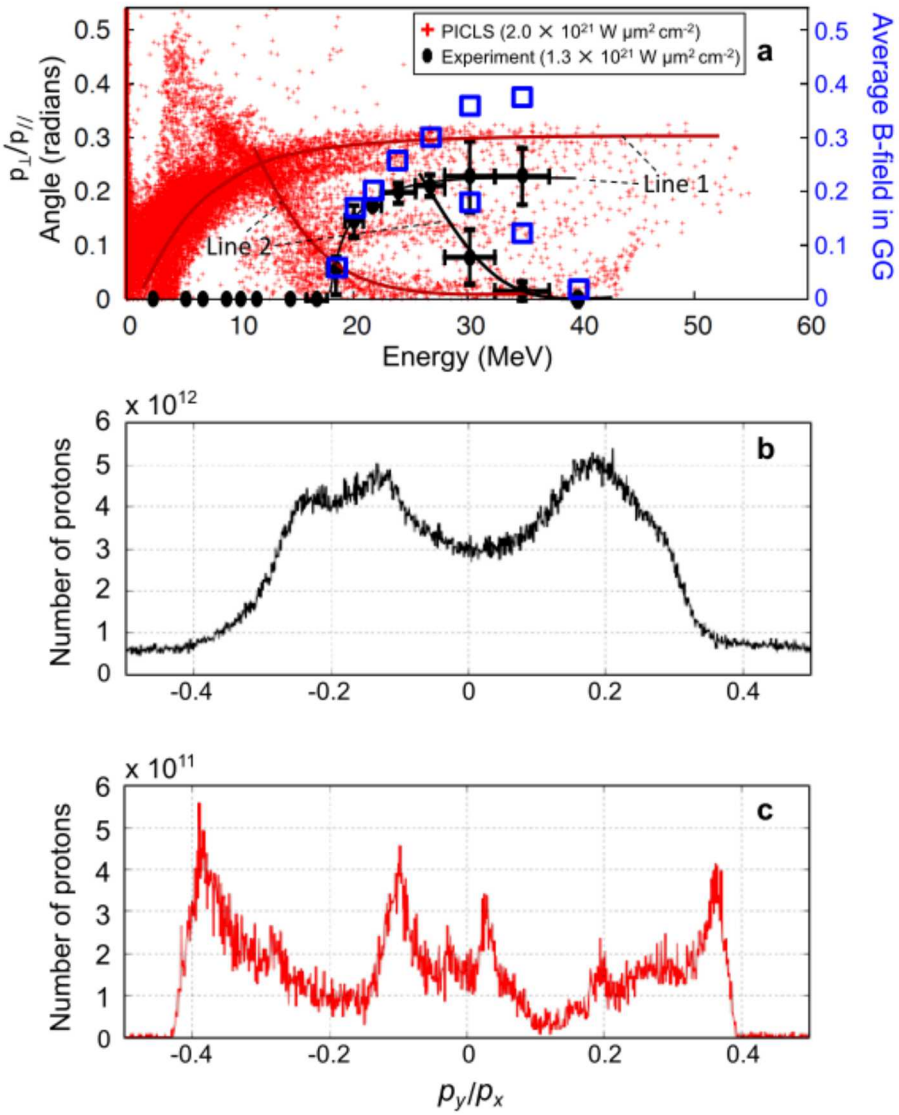

Supplementary Figure 4: Angle-energy proton distributions. (**a**) Red small dots are from a 2D PICLS simulation performed at a 2×10^{21} W μm^2 cm^{-2} intensity (see Fig. 4.b of the main text), measured 300 fs after the laser peak. Large black dots are experimental results obtained at similar intensity (see Fig. 4f-h of the main text). Blue open squares are the average magnetic field (in GG units) extracted from the experimentally observed angular deflection (see text in detail). (**b**) Angular distribution of low-energy protons (< 10 MeV), obtained from PICADOR simulations performed with the same parameters as in **a**. (**c**) Same as **b** for mid-energy protons ($10 - 20$ MeV).

Supplementary Note 4: Experimental scalings of the maximum proton energy

The plot shown in Supplementary Figure 5 is an update of Fig. 4 of Ref. [1]. The plot compiles data from the following references: (i) [2,3,4,5,6,7,8,9,10,11,12,13] for laser pulse durations between 30 and 100 fs; (ii) [14,15,16,17,18,19,20,21,22,23] for pulse durations between 100 fs and 1 ps; (iii) [24,25] for pulse durations above 1 ps.

The dispersion in the data for a given laser intensity can be attributed to different target and laser parameters (notably, the prepulse level). However, this compilation displays the same trend as in Ref. [2] between ultra-short laser pulses (< 100 fs) and longer pulses: below 10^{19} W μm^2 cm^{-2}, the proton energies obtained with ultra-short pulses (< 100 fs) are clearly below those achieved with longer pulses, while they progressively become of the same order, and possibly higher, above 10^{20} W μm^2 cm^{-2}.

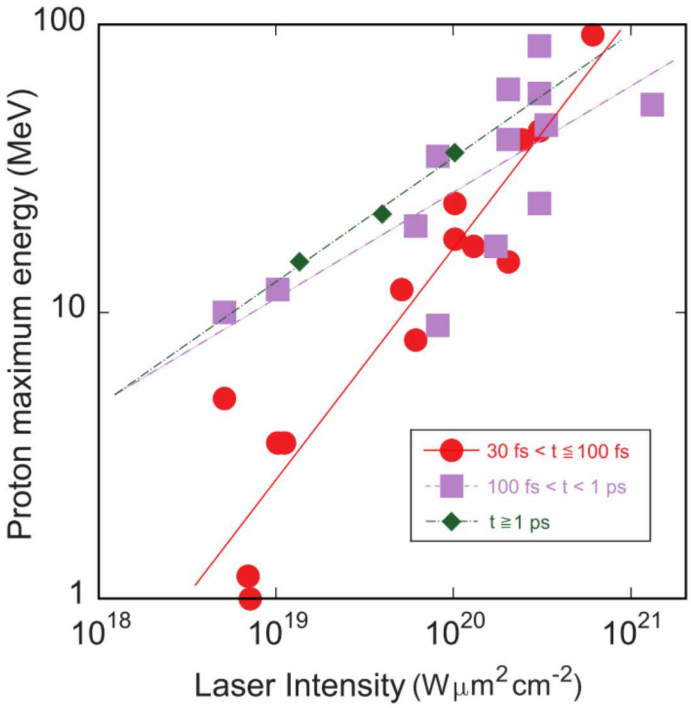

Supplementary Figure 5: Maximum proton energy vs. on-target laser intensity. Compilation of experimental data obtained using various laser facilities and grouped according to the laser pulse duration (denoted "t" in the legend).

Supplementary Note 5: Proton acceleration in the ultra-high-intensity ultra-short-pulse interaction regime

In Supplementary Figure 6 are shown additional PIC simulations, the aim of which is to show that, for few-cycle laser pulses interacting with nanometer-size foils, no significant B-field develops on the target surfaces and that the radiation-pressure mechanism is able to accelerate ions (here H^+ and C^{6+}) to very high energies, in contrast to the simulations presented in the rest of the paper, which employed longer laser pulses and thicker targets.

These 2D simulations were performed using the CALDER code [26]. The simulation domain has dimensions $30000\Delta x \times 8000\Delta y$ with mesh sizes $\Delta x = 1.3$ nm and $\Delta y = 6.4$ nm. The laser pulse, of 0.8 μm wavelength, is Gaussian in space and time, with 1.9 μm spot size and 15 fs duration (FWHM). The peak intensity is either $I_\mathrm{L} = 5 \times 10^{21}$ W cm^{-2} or $I_\mathrm{L} = 1.8 \times 10^{22}$ W cm^{-2}. The target is a 100 nm-thick, fully ionized carbon foil at solid density, coated on both front and rear sides with a Δx-thick H^+ layer. The initial electron and ion temperatures are $T_\mathrm{e} = T_\mathrm{i} = 10$ eV. Collisions and radiation losses are not described. 500 particles are used per cell and species.

The above interaction conditions correspond to the relativistic-transparency regime which is known to optimize ion acceleration [27], and which translates into both significant laser absorption ($\sim 20-25\%$) and reflection ($\sim 30-60\%$) rates. In this regime, ion acceleration results from the combined action of radiation pressure and rear-side sheath field. Maximum proton energies of 120 MeV and 250 MeV are reached for $I_\mathrm{L} = 5 \times 10^{21}$ W cm^{-2} and 1.8×10^{22} W cm^{-2}, respectively. Because the electrons keep on being accelerated (reaching mean energies of $\sim 5-10$ MeV for the two intensities considered) as part of the laser pulse shines through the foil, they are less affected by the magnetostatic field, whose peak strength is measured to be in the $0.5-1$ GG range when proton acceleration starts saturating. Consequently, the hot-electron density does not exhibit any depletion off axis, in contrast to what is observed in Supplementary Fig. 1. Also, the B-field peaks quite far away transversely from the central region where the ion acceleration takes place, causing the ion density patterns shown in Supplementary Figure 6 (evolving into mushroom-shaped profiles at later times).

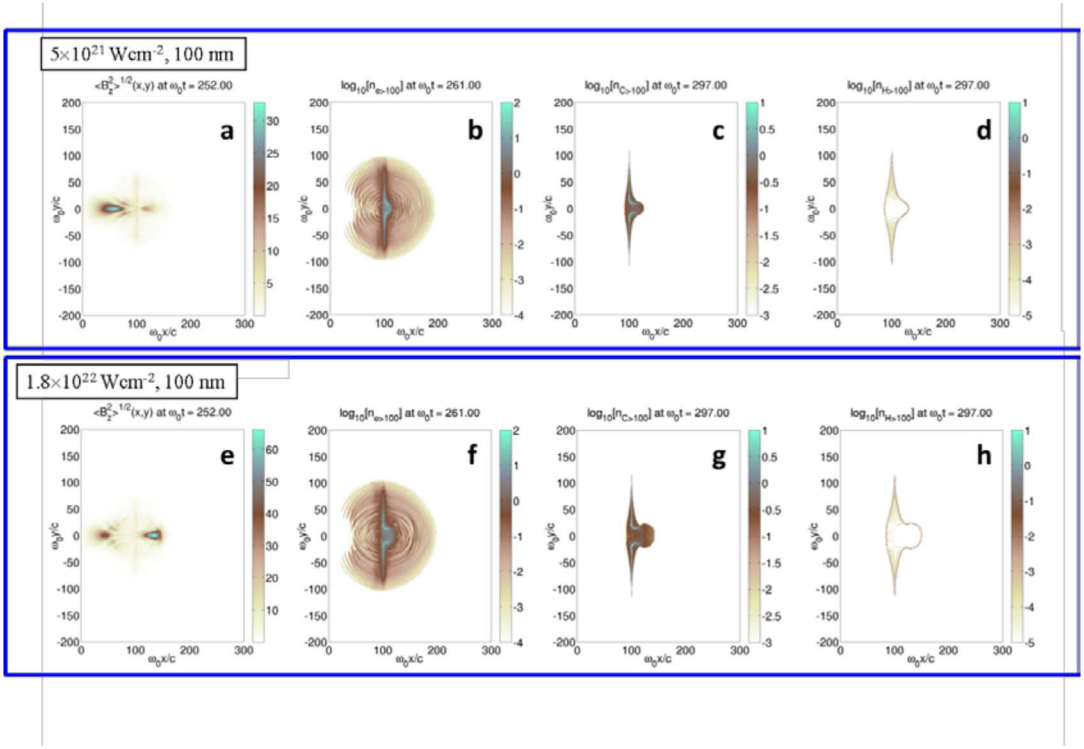

Supplementary Figure 6: Proton acceleration from sub-micron targets driven by ultra-high-intensity ultra-short lasers. 2D CALDER PIC simulation of the interaction of 15 fs laser pulses of intensity (**a**-**d**) $I_{\mathrm{L}} = 5 \times 10^{21}\ \mathrm{W\ cm^{-2}}$ and (**e**-**g**) $I_{\mathrm{L}} = 1.8 \times 10^{22}\ \mathrm{W\ cm^{-2}}$ with a 100 nm-thick carbon foil. (**a**,**e**) Quadratic average of the B-field, $\langle B_Z^2 \rangle^{1/2}$ (in units of 100 MG $= 10^4$ T, note that the strong peak corresponds to the laser field). (**b**,**f**) Density (in units of $10^{21}\ \mathrm{cm^{-3}}$) of electrons of kinetic energies > 100 keV. (**c**,**g**) Density of carbon ions of kinetic energies > 100 keV. (**d**,**h**) Density of protons of kinetic energies > 100 keV. Space and time coordinates are in units of $c/\omega_0 = 0.16\ \mu$m and $\omega_0^{-1} = 0.53$ fs, respectively (ω_0 is the angular laser frequency). The on-target peak intensity is reached at $t = 205\omega_{\mathrm{L}}^{-1}$. The title of each figure indicates the time at which it is recorded. The ion density maps are shown at the saturation time for ion acceleration.

Supplementary Note 6: Model-predicted laser dependence of the B-field strength

Supplementary Figure **7** displays the variation of the B-field with the laser spot size, as predicted by our 1-D model. To calculate it, we first introduce the characteristic time, t_{char}, when the expanding protons have moved a distance equal to the local Debye length. From the model, this characteristic time appears to be about twice the inverse plasma ion frequency, $\omega_{\mathrm{pi}}^{-1}$.

Supplementary Figure **7**b shows that t_{char} depends on the laser intensity, but also the laser spot size. This is due to the fact that, for a given hot electron divergence (a 45° half angle is used here) and target thickness (2 μm), hot electron dilution occurs faster at smaller spot sizes.

Supplementary Figure **7**a explains how the lateral spread of the hot electrons due to recirculation is estimated at $t = t_{\mathrm{char}}$, yielding the sheath diameter, $2r$. Then, the magnetic field strength, $B_z(t)$, follows from time integrating the sheath electric field $E_x(t)$ divided by the sheath radius r.

Supplementary Figure **7**d plots the B-field strength at the laser intensity peak, $B_z(t_{\mathrm{max}})$. Note that its maximum value is limited to $B_{\mathrm{max}} \equiv \left(2\mu_0 n_{\mathrm{h,rear}} k_{\mathrm{B}} T_0\right)^{1/2}$. It appears that moderate spot sizes ($\phi_{\mathrm{L}} = 4 - 10$ μm) give slightly stronger B-fields than at tight focusing ($\phi_{\mathrm{L}} = 0.9$ μm). Only when the spot size becomes comparable with the sheath size, does the B-field start to decrease.

Overall, this implies that the magnetic inhibition highlighted in our present study, using tight focusing in order to access high laser intensities, will likely be even stronger under more standard focusing conditions (e.g. $\phi_{\mathrm{L}} = 4 - 10$ μm).

Supplementary Figure **8** illustrates the model-predicted dependency of the B-field against the laser pulse duration. Although shorter pulse durations lead to smaller magnetic fields (due to the finite growth rate of the B-field, as further discussed in Supplementary Note 7), strong magnetic fields of few 100 MG are predicted for laser intensities $> 10^{21}$ W cm^{-2}, even for 50 fs duration pulses. However, Supplementary Figure **8**b shows that the electron magnetization (quantified by the ratio of the electron Larmor radius and the acceleration front), and therefore the magnetic inhibition of

proton acceleration, is reduced when shortening the pulse duration down to $\tau_L = 50$ fs. In short, this clearly shows the benefit of using laser shorter pule durations to lessen the magnetic inhibition highlighted in our study.

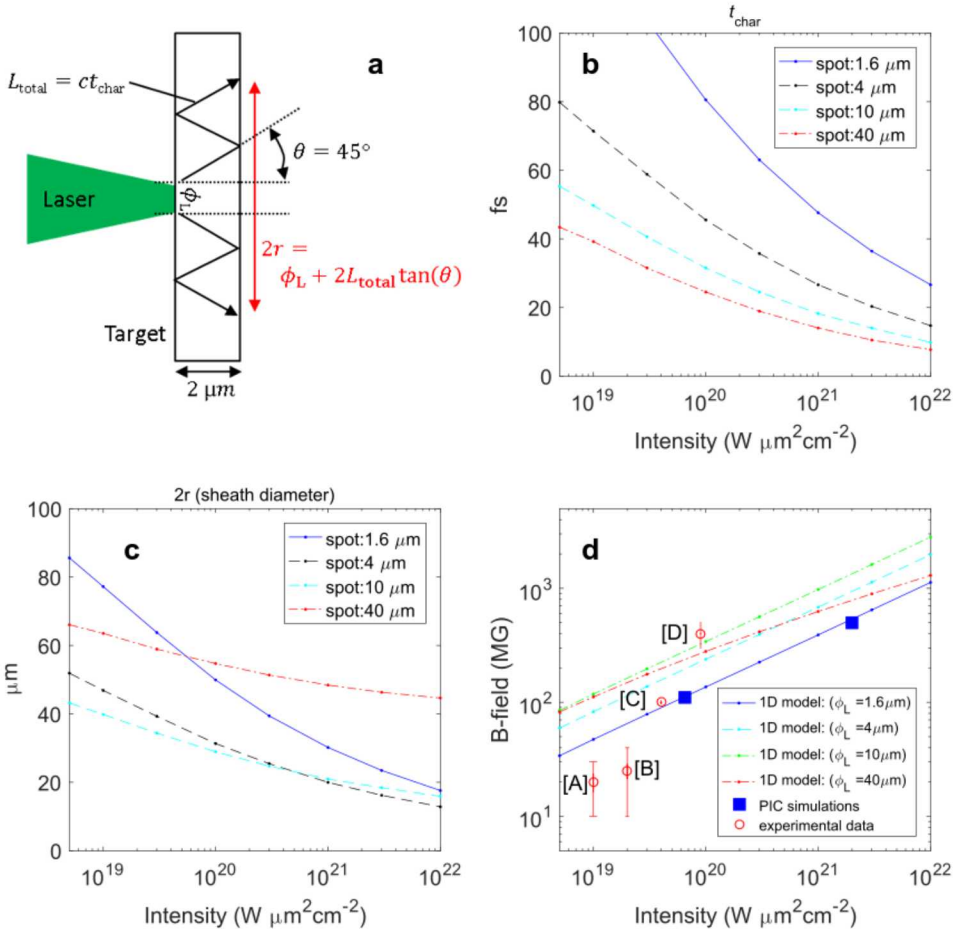

Supplementary Figure 7: Model-predicted variation of the B-field strength with the laser spot size. (**a**) Schematic drawing to show the lateral spread of the hot electrons due to recirculation is estimated at $t = t_{\mathrm{char}}$, yielding the sheath diameter, $2r$. (b) Characteristic time t_{char} when the plasma expansion starts, defined as the time when the front protons have moved a distance equal to the local Debye length. (**c**) Sheath diameter at $t = t_{\mathrm{char}}$ due to fast electron recirculation and transverse spread. (**d**) Magnetic field strength calculated for various laser spot sizes and laser peak intensities, taken at the laser intensity peak. For all curves, the laser wavelength is $\lambda_{\mathrm{L}} = 1\ \mu$m. The red circles correspond to experimental observations ([A] G. Sarri et al., Phys. Rev. Lett. **109**, 205002 (2012), [B] B. Albertazzi et al., Phys. Plasmas **22**, 123108 (2015), [C] W. Schumaker et al., Phys. Rev. Lett. **110**, 015003 (2013), [D] M. Tatarakis et al. Nature **415**, 280 (2002)), while the blue boxes come from the PIC simulations of the paper (see Fig.1 of the main text).

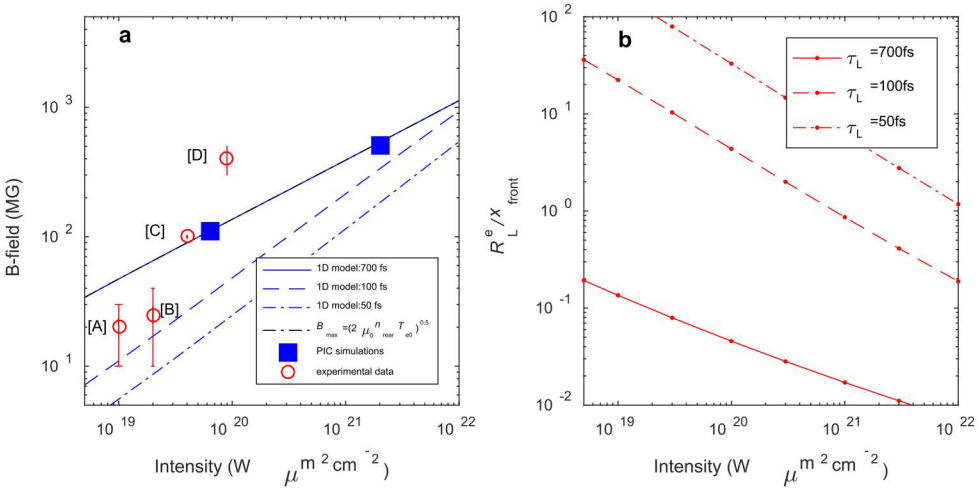

Supplementary Figure 8: Model-predicted variations of the B-field strength and electron magnetization level with the laser pulse duration. (**a**) B-field (in MG units) at the laser intensity peak (**b**) Normalized electron Larmor radius $R_{\mathrm{L}}^{\mathrm{e}}/x_{\mathrm{front}}$ at the laser intensity peak. The laser spot size and wavelength are $\phi_{\mathrm{L}} = 1.6\ \mu$m and $\lambda_{\mathrm{L}} = 1\ \mu$m, respectively.

Supplementary Note 7: Proton acceleration and electron magnetization with a 50 fs laser pulse

Supplementary Figure 9 displays the results of a PIC simulation run with a laser pulse of duration (50 fs) much shorter than that used in the highest-intensity case discussed in the main text (800 fs, at SNL). The other laser parameters were kept equal to those used in Fig. 1e of the main text (i.e., $I_{\mathrm{L}} = 2 \times 10^{21}$ W μm^{2}cm^{-2}, $\phi_{\mathrm{L}} = 1.6\ \mu$m and $\lambda_{\mathrm{L}} = 1\ \mu$m). This simulation, performed with the PICADOR code (see Methods), aims to show that the reduction in the acceleration timescale that results from a shorter laser pulse weakens the magnetization effects on proton acceleration. When comparing the simulation results with 50 fs and 700 fs pulse durations, several points can be noticed: (i) In the 50 fs case, the generated magnetic field at the peak of the laser pulse is the same order. (ii) Similar electron energies are reached (which was rather expected since the laser intensities are the same). (iii) Similar maximum proton energies are attained, although a slightly higher value is found for a 50 fs pulse, consistent with previous researches (Supplementary Fig. 7).

Since in the 50 fs case, the laser intensity reaches its maximum much quicker, the protons reach their saturation energy over a much shorter distance, and hence the sheath longitudinal length is shorter than for a 700 fs pulse. It is in fact even shorter than the electron Larmor radius over the timescale of proton acceleration, so that the electrons are weakly magnetized in the 50 fs case, even though the magnetic field strength are similar for both pulse durations (compare Supplementary Figure 9c and Fig. 1b in the main text).

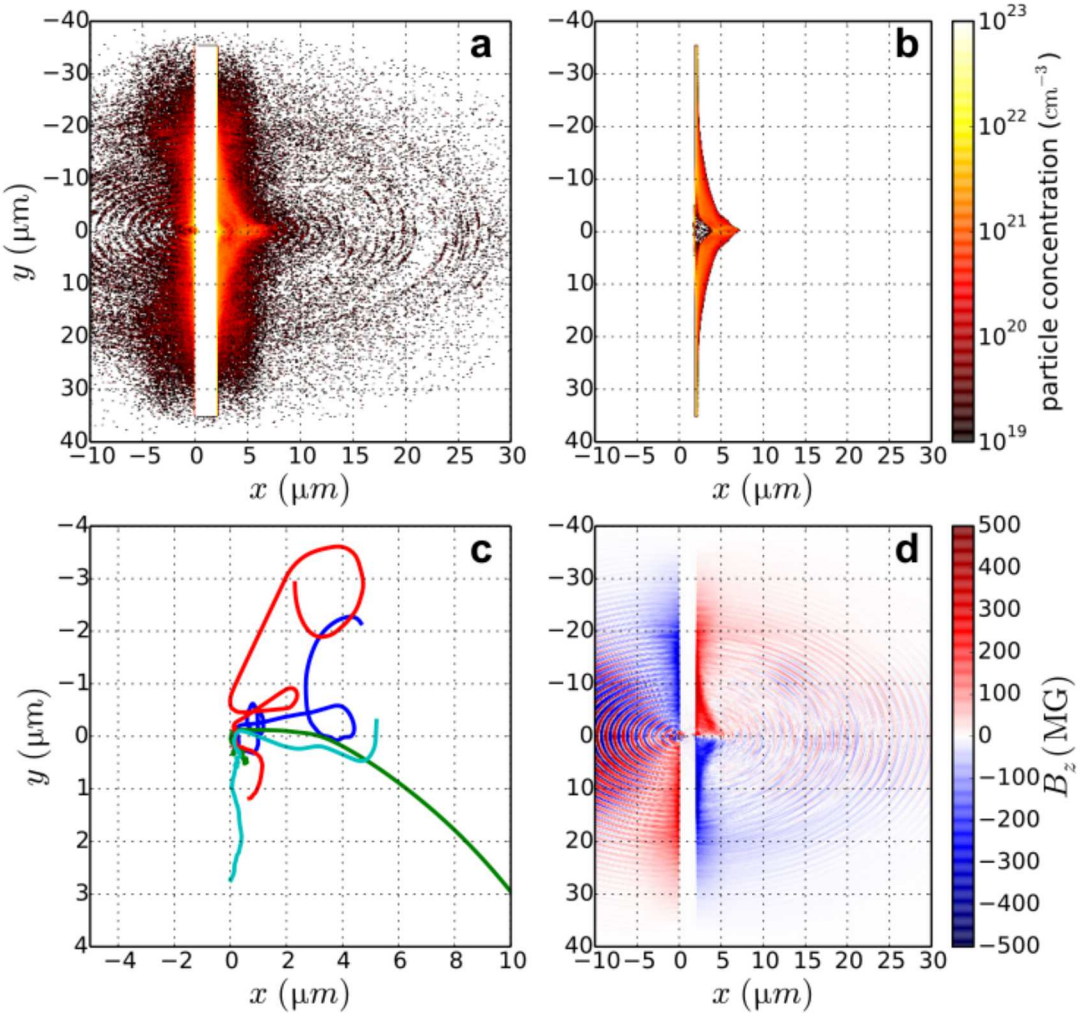

Supplementary Figure 9: Proton acceleration at high intensity by a 50 fs laser pulse. 2D PICADOR PIC simulation of a 50 fs laser pulse of intensity $I_{\mathrm{L}} = 2 \times 10^{21}$ W cm^{-2}, spot size $\phi_{\mathrm{L}} = 1.6$ μm and wavelength $\lambda_{\mathrm{L}} = 1$ μm interacting with a 2 μm thick Al foil coated with a 20 nm thick proton layer on its rear side. Shown are the (**a**) electron and (**b**) ion densities (in cm^{-3} units), (**c**) trajectories of sampled energetic electrons, and (**d**) the transverse magnetic field, B_{z} (in MG units). All snapshots are taken at the laser intensity peak.

Supplementary Note 8: Proton acceleration and electron magnetization in a reduced mass target

In Supplementary Figure **10** are shown the results of an additional PICADOR PIC simulation performed with a small-width target (i.e., a so-called reduced mass target, RMT). The laser parameters are those used in Fig. 1e in the main text, *i.e.*, $\tau_{\mathrm{L}} = 700$ fs, $\phi_{\mathrm{L}} = 1.6\,\mu$m, $I_{\mathrm{L}} = 2 \times 10^{21}$ W cm^{-2}. The target is similar to that considered in Fig. 1 except that its transverse width is reduced to 20 μm. The purpose of this simulation is to demonstrate that proton acceleration in RMTs is still affected by magnetization effects.

In this case, it is seen that the transverse gradients of the magnetic field on the target rear side are smaller than when using a large target (as in Fig. 1 of the main text). However, the field itself is comparable in strength and topology with that in a large target. This may contradict the intuitive view that reducing the target transverse size makes the electron sheath flatter, thus reducing the inductive B-field generated by the transverse gradient of the sheath electric field via $\partial B_z/\partial t \propto \partial E_x/\partial y$. However, the magnetic field is also produced by $\partial E_y/\partial x$ gradients, which can be greater in RMTs. Indeed, whilst the longitudinal scales are then close to those found in large targets, the transverse electric field is somewhat greater due to denser hot electrons.

Generally speaking, the B-field generation at the target rear side follows from the hot electrons expelled by the laser pulse. They form an electric current on axis, which is actually the original source of the magnetostatic field. The electric fields involved in the time-dependent Faraday law can be seen as an intermediate step between the current and the magnetic field, which determine the steady growth of the magnetic field up to the stage when the magnetic pressure becomes comparable with the plasma pressure. From simulations, we estimated the current intensity and the magnitude of the magnetic field and found that, close to the target rear surface, they are consistent with the quasistatic Ampere's law $\nabla \times \mathbf{B} = \mu_0 \mathbf{J}$. The current intensity, in turn, depends only on the number and velocities of the laser-driven hot electrons, both depending on the laser intensity and target density, rather than on the target geometry. This is the reason why the B-field strength is weakly sensitive to the transverse target width.

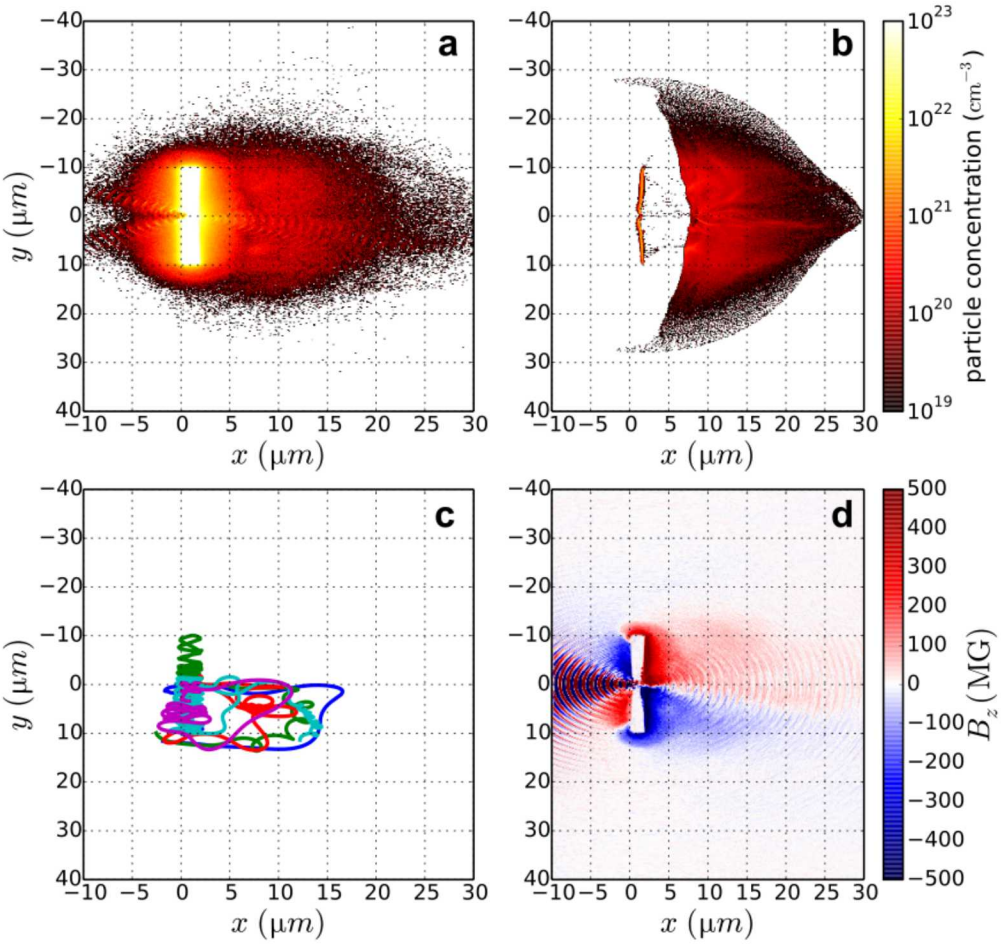

Supplementary Figure 10: Proton acceleration at high laser intensity in a reduced mass target. 2D PICADOR PIC simulation of a 700 fs laser pulse of intensity $I_{\mathrm{L}} = 2 \times 10^{21}$ W cm^{-2}, spot size $\phi_{\mathrm{L}} = 1.6\ \mu$m and wavelength $\lambda_{\mathrm{L}} = 1\ \mu$m interacting with an Al foil of 2 μm thickness and 20 μm transverse size, coated with a 20 nm thick proton layer on its rear side. Shown are the (**a**) electron and (**b**) ion densities (in cm^{-3} units), (c) trajectories of sampled energetic electrons, and (**d**) the transverse magnetic field, B_z (in MG units). All snapshots are taken at the laser intensity peak.

This magnetic field is strong enough to magnetize electrons as can be seen from the electron trajectories shown in Supplementary Figure **10**c. As a consequence, it acts detrimentally on proton acceleration (through the same mechanisms as described in the manuscript). This explains why RMTs yield only a modest increase in proton energies compared to large targets and why, even at very high intensities ($> 10^{21}$ W cm^{-2}), they do not give rise to the proton acceleration level predicted by the simple 1D, unmagnetized model.

Supplementary Note 9: Sensitivity of ellipsoid plasma mirror focusing to plasma expansion

The peak laser intensity on the ellipsoid plasma mirror (EPM) surface was about $3 \times 10^{14} - 5 \times 10^{14}$ W cm^{-2} for both the LULI and SNL experiments. This yielded a cumulated fluence on the plasma mirror surface of $F \simeq 130 - 180$ J cm^{-2} around the pulse maximum, and of $F \simeq 280 - 370$ J cm^{-2} at the end of the pulse (*i.e.*, at $t = \tau_L$ after the laser intensity peak). The time-dependent plasma temperature T_e at the critical-density surface of the SiO_2 material composing the EPM approximately varies as $T_e(\text{eV}) \simeq F(\text{J cm}^{-2})$ [28]. This simple scaling allows one to infer the expansion of the critical-density surface, as shown in Supplementary Figure 11. The expansion length is predicted to be of 0.07 μm around the laser peak, and of 0.19 μm at the end of the pulse.

Ray-trace simulations were performed to assess the effect of this surface expansion on the focusing quality of the EPM (Supplementary Fig. 12). Within the $f/4$ laser cone incoming into the EPM, we selected 71 rays with a 0.2° angular step. The plasma was assumed to expand normally to the EPM surface. The ray-trace calculations reveal that the plasma expansion is too weak to degrade significantly the final spot size. Even for a much larger ($> 10\times$) expansion length (2 μm), the spot size at the second focus of the EPM is significantly smaller than the diffraction limited size. Hence, for our laser parameters, the surface expansion of the EPM is not expected to affect our results.

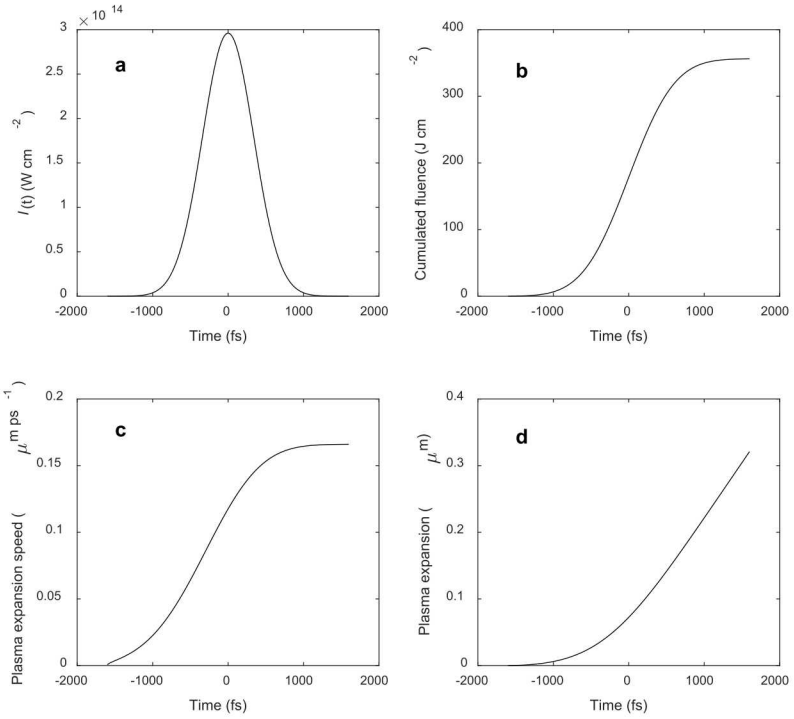

Supplementary Figure 11: Predicted expansion of the critical-density surface of the EPM. The laser parameters are those of the highest-fluence SNL experiment: 90 J on-target laser energy, 1 μm wavelength, 800 fs duration and the beam diameter on the plasma mirror surface is $5/\cos\theta$ mm, with $\theta = 39°$. The expansion length is predicted to be of ~ 0.07 µm around the laser peak and ~ 0.19 µm at the end of the pulse, i.e., when the laser intensity reaches $I(t = 800\ \text{fs}) \sim 0.06 I_{\text{L}}$. Shown are the temporal evolutions of **(a)** the laser intensity on the EPM surface, **(b)** cumulated fluence (in J cm^{-2} units), **(c)** expansion velocity of the critical-density surface (in μm ps^{-1} units) and (**d**) plasma expansion length (in μm units). The expansion velocity is estimated to be $c_{\text{s}} = \sqrt{Z_{\text{eff}} T_{\text{e}} / A m_{\text{p}}}$ with A the atomic mass, m_{p} the proton mass and an ionization state $Z_{\text{eff}} / Z = 0.7$, assuming all the electrons except the 1s and 2s of Si and O are ionized. The electron temperature at the expanding surface is supposed to vary as T_{e} (eV) $\approx F$(J cm^{-2}) [28].

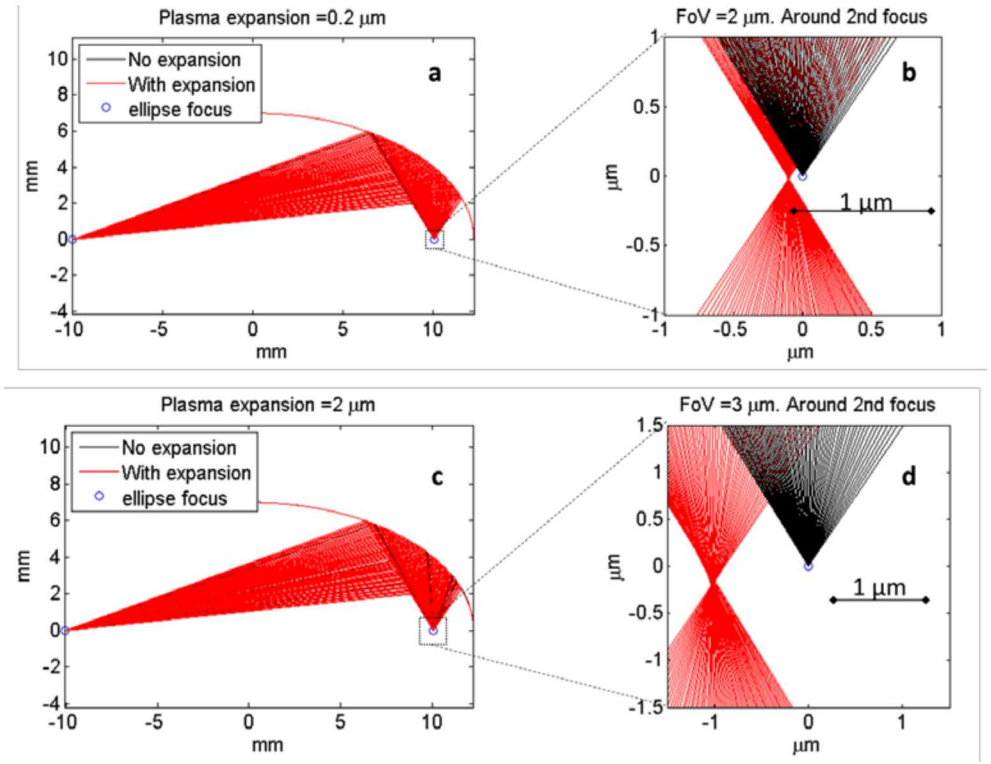

Supplementary Figure 12: Ray-tracing simulation of the EPM focusing in the geometrical optics approximation. In (**a**, **b**), the reflection surface is shifted by 0.2 μm along the local normal of the ellipsoid to take into account the surface expansion. **b** is a zoom of **a** around the second focus of the ellipsoid. The resulting focal spot is, however, significantly smaller than the diffraction-limited spot size ($\sim$ 1 μm). Black rays are reference rays in the absence of plasma expansion, thus they focus to an infinitively small spot. In (**c**, **d**) an exaggerated 2 μm expansion length is considered. The resulting spot size is still smaller than 1 μm, which demonstrates the robustness of the EPM against plasma expansion during the pulse. In all cases, the incident rays are fixed.

SUPPLEMENTARY REFERENCES

1 Macchi, A., Borghesi, M., and Passoni, M. Ion acceleration by superintense laser-plasma interaction. *Reviews of Modern Physics* **85**, 751-793 (2013).

2 Spencer, I. , Ledingham, K. W. D., McKenna, P., McCanny, T., Singhal, R. P., Foster, P. S., Neely, D., Langley, A. J., Divall, E. J., Hooker, C. J., Clarke, R. J., Norreys, P. A., Clark, E. L., Krushelnick. K., and Davies, J. R., Experimental study of proton emission from 60-fs, 200-mJ high-repetition-rate tabletop-laser pulses interacting with solid targets, *Phys. Rev. E* **67**, 046402 (2003).

3 Fritzler, S. *et al.*, Proton beams generated with high-intensity lasers: Applications to medical isotope production, *App. Phys. Lett.* **83**, 3039-3041 (2003).

4 Fuji, T. *et al.*, MeV-order proton and carbon ion acceleration by irradiation of 60 fs TW laser pulses on thin copper tape, *App. Phys. Lett.* **83**, 1524-1526 (2003).

5 Mackinnon, A. J. *et al.*, Enhancement of Proton Acceleration by Hot-Electron Recirculation in Thin Foils Irradiated by Ultraintense Laser Pulses, *Phys. Rev. Lett.* **88**, 215006 (2002).

6 Oishi, Y. *et al.*, Dependence on laser intensity and pulse duration in proton acceleration by irradiation of ultrashort laser pulses on a Cu foil target, *Phys. Plasmas* **12**, 073102 (2005).

7 Zeil, K., Kraft, S. D., Bock, S., Bussmann, M., Cowan, T. E., Kluge, T., Metzkes, J., Richter, T., Sauerbrey, R., and Schramm, U., The scaling of proton energies in ultrashort pulse laser plasma acceleration, *New J. Phys.* **12**, 045015 (2010).

8 Ogura, K. *et al.,* Proton acceleration to 40 MeV using a high intensity, high contrast optical parametric chirped-pulse amplification/Ti:sapphire hybrid laser system, *Optics Letters* **37**, 2868-2870 (2012).

9 Burdonov, K. F., Eremeev, A. A., Ignatova, N. I., Osmanov, R. R., Sladkov, A. D., Soloviev, A. A., Starodubtsev, M. V., Ginzburg, V. N, Kuz'min, A. A., Maslennikova, A. V., Revet, G., Sergeev, A. M., Fuchs, J., Khazanov, E. A., Chen, S., Shaykin, A. A., Shaikin, I. A., and Yakovlev, I. V., Experimental stand for studying the impact of laser-accelerated protons on biological objects, *Quantum Electronics* **46**, 283-287 (2016).

10 Ceccotti, T., Lévy, A., Popescu, H., Réau, F., D'Oliveira, P., Monot, P., Geindre, J. P., Lefebvre, E., and Martin, Ph. Proton Acceleration with High-Intensity Ultrahigh-Contrast Laser Pulses, *Phys. Rev. Lett.* **99**, 185002 (2007).

11 Kim, I. J., Pae, K. H., Choi, I. W., Lee, C. -L., Kim, H. T., Singhal, H., Sung, J. H., Lee, S. K., Lee, H. W., Nickles, P. V., Jeong, T. M., Kim, C. M., and Nam, C. H. Radiation pressure acceleration of protons to 93 MeV with circularly polarized petawatt laser pulses, *Phys. Plasmas* **23**, 070701 (2016).

12 Dollar, F., Zulick, C., Thomas, A. G. R., Chvykov, V., Davis, J., Kalinchenko, G., Matsuoka, T., McGuffey, C., Petrov, G. M., Willingale, L., Yanovsky, V., Maksimchuk, A., and Krushelnick, K. Finite Spot Effects on Radiation Pressure Acceleration from Intense High-Contrast Laser Interactions with Thin Targets, *Phys. Rev. Lett.* **108**, 175005 (2012).

13 Henig, A., Steinke, S., Schnürer, M., Sokollik, T., Hörlein, R., Kiefer, D., Jung, D., Schreiber, J., Hegelich, B. M., Yan. X. Q., Meyer-ter-Vehn, J., Tajima, T., Nickles, P. V., Sandner W., and Habs, D. Radiation-Pressure Acceleration of Ion Beams Driven by Circularly Polarized Laser Pulses, *Phys. Rev. Lett.* **103**, 245003 (2009).

14 Murakami, Y. *et al.*, Observation of proton rear emission and possible gigagauss scale magnetic fields from ultra-intense laser illuminated plastic target, *Phys. Plasmas* **8**, 4138-4143 (2001).

15 McKenna, P., Ledingham, K. W. D., Yang, J. M., Robson, L., McCanny, T., Shimizu, S., Clarke, R. J., Neely, D., Spohr, K., Chapman, R., Singhal, R. P., Krushelnick, K., Wei, M. S., and Norreys, P. A. Characterization of proton and heavier ion acceleration in ultrahigh-intensity laser interactions with heated target foils, *Phys. Rev. E* **70**, 036405 (2004).

16 Maksimchuk, A. *et al.*, High-energy ion interactions by short laser pulses, *Plasma Phys. Reports* **60**, 473 (2004).

17 Snavely, R. A. *et al.*, Intense High-Energy Proton Beams from Petawatt-Laser Irradiation of Solids, *Phys. Rev. Lett.* **85**, 2945-2948 (2000).

18 Fuchs, J., Antici, P., D'Humieres, E., Lefebvre, E., Borghesi, M., Brambrink, E., Cecchetti. C. A., Kaluza, M., Malka, V., Manclossi, M., Meyroneinc, S., Mora, P., Schreiber, J., Toncian, T., Pepin, H., and Audebert, P. Laser-driven proton scaling laws and new paths towards energy increase, *Nat. Phys.* **2**, 48-54 (2006).

19 Bartal, T., Foord, M. E., Bellei, C., Key, M. H., Flippo, K. A., Gaillard, S. A., Offermann, D. T., Patel P. K., Jarrott, L. C., Higginson, D. P., Roth, M., Otten, A., Kraus, D., Stephens, R. B., McLean, H. S., Giraldez, E. M., Wei, M. S., Gautier D. C., and Beg, F. N. Focusing of short-pulse high-intensity laser-accelerated proton beams, *Nat. Phys.* **8**, 139–142 (2012).

20 Wagner, F., Deppert, O., Brabetz, C., Fiala, P., Kleinschmidt, A., Poth, P., Schanz, V. A., Tebartz, A., Zielbauer, B., Roth, M., Stöhlker, T., and Bagnoud, V. Maximum Proton Energy above 85 MeV from the Relativistic Interaction of Laser Pulses with Micrometer Thick CH2 Targets, *Phys. Rev. Lett.* **116**, 205002 (2016).

21 Henig, A., Kiefer, D., Markey, K., Gautier, D. C., Flippo, K. A., Letzring, S., Johnson, R. P., Shimada, T., Yin, L., Albright, B. J., Bowers, K. J., Fernandez, J. C., Rykovanov, S. G., Wu, H. -C., Zepf, M., Jung, D., Liechtenstein, V. Kh., Schreiber, J., Habs, D., and Hegelich, B. M. Enhanced

Laser-Driven Ion Acceleration in the Relativistic Transparency Regime, *Phys. Rev. Lett.* **103**, 045002 (2009).

22 Kar, S., Kakolee, K. F., Qiao, B., Macchi, A., Cerchez, M., Doria, D., Geissler, M, McKenna, P., Neely, D., Osterholz, J., Prasad, R., Quinn, K., Ramakrishna, B., Sarri, G., Willi, O., Yuan, X. Y., Zepf, M., and Borghesi, M. Ion Acceleration in Multispecies Targets Driven by Intense Laser Radiation Pressure, *Phys. Rev. Lett.* **109**, 185006 (2012).

23 Hornung, M., Keppler, S., Liebetrau, H., Kessler, A., Seidel, A., Hellwing, M., Schorcht, F., Körner, J., Sävert, A., Polz, J., Becker, G., Arunachalam, A. K., Klöpfel, D., Hein, J., and Kaluza, M. C. Status of the POLARIS laser system, 8th workshop on High-Energy-Class Diode-Pumped Solid-State Lasers, Oxford, 26th March 2014, http://www.clf.stfc.ac.uk/clf/resources/pdf/talk_1.pdf.

24 Spencer, I., Ledingham, K. W. D., Singhal, R. P., McCanny, T., McKenna, P., Clark, E. L., Krushelnick, K., Zepf, M., Beg, F. N., Tatarakis, M., Dangor, A. E., Norreys, P. A., Clarke, R. J., Allott, R. J., and Ross, I. N. Laser generation of proton beams for the production of short-lived positron emitting radioisotopes, *Nucl. Instrum. Meth. B*, **183**, 449-458 (2001).

25 Zepf, M., Clark, E. L., Krushelnick, K., Beg, F. N., Escoda, C., Dangor, A. E., Santala, M. I. K., Tatarakis, M., Watts I. F., Norreys, P. A., Clarke, R. J, Davies, J. R., Sinclair M. A., Edwards, R. D., Goldsack, T. J., Spencer, I., and Ledingham K. W. D. Fast particle generation and energy transport in laser-solid interactions, *Phys. Plasmas* **8**, 2323-2330 (2001).

26 Lefebvre, E. *et al*. Electron and photon production from relativistic laser–plasma interactions. *Nucl. Fusion* **43**, 629-633 (2003).

27 Esirkepov, T., Yamagiwa, M., and Tajima, T. Laser Ion-Acceleration Scaling Laws Seen in Multiparametric Particle-in-Cell Simulations. *Phys. Rev. Lett.* **96,** 105001 (2006).

28 Doumy, G. *et al*. Complete characterization of a plasma mirror for the production of high-contrast ultraintense laser pulses. *Phys. Rev. E* **69**, 026402 (2004).